JGR Atmospheres

RESEARCH ARTICLE
10.1029/2023JD039324

Ice Supersaturation Variability in Cirrus Clouds: Role of Vertical Wind Speeds and Deposition Coefficients

B. Kärcher[1], E. J. Jensen[2], G. F. Pokrifka[3], and J. Y. Harrington[3]

[1]Institut für Physik der Atmosphäre, DLR Oberpfaffenhofen, Wessling, Germany, [2]National Oceanic and Atmospheric Administration (NOAA), Earth System Research Laboratories, Boulder, CO, USA, [3]Department of Meteorology and Atmospheric Science, The Pennsylvania State University, University Park, PA, USA

Key Points:

- This study presents a process-based, systematic investigation of key factors controlling ice supersaturation statistics within cirrus
- Gravity wave-induced mesoscale temperature fluctuations cause a remarkably large variability in ice supersaturation
- Ice supersaturation statistics are not strongly modified by depositional growth with supersaturation-dependent deposition coefficients

Correspondence to:

B. Kärcher,
bernd.kaercher@dlr.de

Citation:

Kärcher, B., Jensen, E. J., Pokrifka, G. F., & Harrington, J. Y. (2023). Ice supersaturation variability in cirrus clouds: Role of vertical wind speeds and deposition coefficients. *Journal of Geophysical Research: Atmospheres*, *128*, e2023JD039324. https://doi.org/10.1029/2023JD039324

Received 26 MAY 2023
Accepted 28 OCT 2023

Author Contributions:

Conceptualization: B. Kärcher
Formal analysis: B. Kärcher, E. J. Jensen, G. F. Pokrifka, J. Y. Harrington
Investigation: B. Kärcher, E. J. Jensen, G. F. Pokrifka, J. Y. Harrington
Methodology: B. Kärcher, E. J. Jensen, G. F. Pokrifka, J. Y. Harrington
Software: B. Kärcher
Validation: B. Kärcher
Writing – original draft: B. Kärcher
Writing – review & editing: B. Kärcher, E. J. Jensen, G. F. Pokrifka, J. Y. Harrington

Abstract Aircraft measurements reveal ice supersaturation statistics in cirrus (ISSs) with broad maxima around ice saturation and pronounced variance. In this study, processes shaping ISSs in midlatitude and tropical upper tropospheric conditions are systematically investigated. Water vapor deposition and sublimation of size-resolved ice crystal populations are simulated in an air parcel framework. Mesoscale temperature fluctuations (MTFs) due to gravity waves force the temporal evolution of supersaturation. Various levels of background wave forcing and cirrus thickness are distinguished in stochastic ensemble simulations. Kinetic limitations to ice mass growth are brought about by supersaturation-dependent deposition coefficients that represent efficient and inefficient growth modes as a function of ice crystal size. The simulations identify a wide range of deposition coefficients in cirrus, but most values stay above 0.01 such that kinetic limitations to water uptake remain moderate. Supersaturation quenching times are long, typically 0.5–2 hr. The wave forcing thus causes a remarkably large variability in ISSs and cirrus microphysical properties except in the thickest cirrus, producing ensemble-mean ISSs in line with in-situ measurements. ISS variance is controlled by MTFs and increases with decreasing cirrus integral radii. In comparison, the impact of ice crystal growth rates on ISSs is small. These results contribute to efforts directed at identifying and solving issues associated with ice-supersaturated areas and non-equilibrium cirrus physics in global models.

Plain Language Summary Measurements show that cold, high cirrus clouds evolve in ice-supersaturated states away from equilibrium, which sets them apart from low-level liquid water clouds. Such cloud states are brought about by rapidly displacing cloudy air parcels in the vertical wind field. The resulting temperature changes cause ice crystals to either grow or shrink in size by uptake or release of water molecules, which, in turn, tends to restore equilibrium. We carefully examine how ice supersaturation and cirrus properties respond to changes in vertical wind speeds for various ice growth models. We show that cloud-scale wave motions determine to a large extent the frequency of occurrence of ice-supersaturated states. The sensitivity to cloud ice growth is much weaker. Our results help interpret atmospheric observations and may improve the representation of cirrus in global models.

1. Introduction

Cirrus clouds form and develop within the confines of ice-supersaturated areas in the upper troposphere and tropopause region, wherein by definition the relative humidity with respect to the ice phase (RHI) exceeds 100%. Formation, extent, and lifetime of these areas are affected by convection, moisture transport, and vertical air motions on different spatial and temporal scales. Seasonal and geographical variations are linked to weather patterns and have been inferred from observations (Dzambo & Turner, 2016; Irvine et al., 2012; Lamquin et al., 2012). Magnitude and variability in RHI is observed to be large in the midlatitude storm tracks and small in the subtropics (Kahn et al., 2009). RHI is generally large near the cold-point tropical tropopause (Jensen et al., 2017; Krämer et al., 2009; Rollins et al., 2016).

While the ice water content in cirrus clouds results from the history of net water vapor uptake on cloud ice crystals along their trajectories, ambient ice supersaturation, defined as $s = (\mathrm{RHI}/100\%) - 1$ and denoting conditions in which ice crystals either grow ($s > 0$), sublimate ($s < 0$), or stay in thermodynamic equilibrium at ice saturation ($s = 0$), is a variable that responds instantly to local changes in the partial pressure of water vapor and air temperature (Korolev & Mazin, 2003). Factors controlling ice supersaturation within cirrus therefore include water vapor

changes due to ice crystal deposition growth and sublimation along with vertical air motion (i.e., temperature) variability. If not otherwise mentioned, ice supersaturation shall refer to growth conditions in this study.

The lifetime of large-scale ice-supersaturated areas may exceed that of the cirrus clouds residing within them, for which the formation and persistence of contrail cirrus provides evidence (Burkhardt et al., 2008). The highly variable cirrus lifetime is limited by ice crystal sublimation and sedimentation. Tropical cirrus cloud systems last on average for (19–30) ± 16 hr based on Lagrangian analysis of satellite-derived water vapor and cloud data (Luo & Rossow, 2004). Midlatitude deep convective systems that last longer than 6 hr are associated with high midtropospheric relative humidity and stronger middle to upper tropospheric wind shear, producing large areas of anvil cirrus (Feng et al., 2012).

In-situ measurements onboard commercial aircraft flying mostly in the midlatitude Northern Hemisphere found ice-supersaturation 13.5% of the time, with a mean value of 15% (Gierens et al., 1999). According to an analysis of long-term (15-year) aircraft measurements, ice supersaturation occurs in the extratropical upper troposphere and tropopause region on average about 17%–36% of the time with significant variability (Petzold et al., 2020). In the tropical tropopause layer (TTL), the highest and coldest regions on Earth inhabited by cirrus, ice supersaturation occurs even more frequently.

More than 80% of ice-supersaturated pathlengths measured along aircraft flight routes are smaller than 10 km (Reutter et al., 2020). A midlatitude aircraft data set based on 1 Hz measurements report even smaller horizontal pathlengths down to 1 km (Diao et al., 2014). Higher frequency (20 Hz) aircraft measurements of TTL cirrus revealed fine structure in cirrus and humidity data at along-track scales as short as 8.5 m (Jensen et al., 2022). These studies point to a significant small-scale (sub-km) heterogeneity of upper tropospheric ice-supersaturated areas.

Unless models fully resolve horizontal scales in the range 1–10 km, vertical wind variability generated by gravity waves (GWs), hence, the magnitude of resulting cloud-scale temperature and supersaturation fluctuations, will be underestimated (Podglajen et al., 2020). A comparison of the European Centre for Medium-Range Weather Forecasts (ECMWF) ERA-Interim reanalysis data set with aircraft measurements showed that the fine structure of, and magnitudes of ice supersaturation within, these areas are not well reproduced (Reutter et al., 2020). Reasons for this deficiency include the coarse spatial resolution on the order of 100 km, the missing sub-grid variability of vertical wind and moisture fields, and possibly a misrepresentation of cirrus ice formation processes and aerosol-cirrus interactions.

Aircraft flying through ice-supersaturated areas produce contrail cirrus clouds. These clouds are an important component of the climate impact of aviation (Lee et al., 2021) and potentially desirable to mitigate (Kärcher, 2018). However, an analysis of a current numerical weather model shows that it cannot predict ISSs, and therefore contrail persistence, with sufficient spatio-temporal accuracy to avoid such regions with confidence (Gierens et al., 2020).

Accurate representation of ice supersaturation on the scale of individual clouds is important to predict cirrus formation and evolution with confidence. Previous studies have emphasized the importance of non-equilibrium ice cloud physics for the representation of cirrus clouds in global models (Kärcher & Burkhardt, 2008). While some of the above-mentioned shortcomings may be remedied by the use of novel global cloud-resolving models with high (1–5 km) horizontal resolution (Satoh et al., 2019), ice supersaturation is affected by microphysical processes that operate on much smaller scales. The relative importance of cloud ice microphysics and cloud-scale dynamical forcing in shaping and affecting ISSs is unclear.

Deposition coefficients describe molecular-level, kinetic limitations to the attachment of water vapor at the surfaces of cloud ice crystals (D. Lamb & Verlinde, 2011). They not only limit vapor growth rates, but also determine the development of ice crystal shapes (habits) and are therefore an important component in simulating the ice content and radiative response of cirrus. Here, we focus on potential growth limitations and employ supersaturation-dependent deposition coefficients conflating two major growth modes (dislocation and step nucleation growth), generalizing the approach used by K. D. Lamb et al. (2022) to analyze laboratory measurements. We thereby provide insights that are needed for improved model simulations and better validation of ice supersaturation and cirrus.

The present study aims at a better understanding of the interplay between local dynamical and microphysical processes affecting ice supersaturation in cirrus. An early study investigated RHI statistics in cirrus and concluded that non-equilibrium states occur in cirrus more often than in warm clouds (Spichtinger et al., 2004). More recently, Zhao and Shi (2023) investigated possible mechanisms that cause a wide range of RHI values in cirrus based on an observational, midlatitude data set and large-ensemble parcel simulations. We take two further steps forward and systematically analyze probability distributions of ice supersaturation in both, midlatitude and TTL cirrus (ice supersaturation statistics, ISSs) regarding (a) their dependence on the strength of GW-induced vertical wind speeds based on measured quasi-Lagrangian fluctuation time series and (b) the supersaturation-dependence of deposition coefficients incorporating the latest experimental findings from laboratory measurements of water vapor uptake on ice crystals.

The paper is organized as follows. We derive ISSs from aircraft measurements in Section 2 that are later used in data-model comparisons. We introduce our microphysical model and its coupling to GWs in Section 3 and describe simulation scenarios in Section 4. Results from idealized simulations are discussed in Section 5 and Section 6 discusses ensemble simulations. We conclude our study in Section 7 by summarizing our results and suggesting future research topics.

2. Aircraft Measurements of Ice Supersaturation

As the upper troposphere is rather dry most of the time, cloud-free ice-supersaturated regions may exhibit one or several maxima at low relative humidities ($s < 0$) (Krämer et al., 2020). The distributions are skewed toward high s-values due to the non-linear temperature-dependence of the ice saturation vapor pressure; in fact, the positive skewness can be explained solely in terms of variability in temperature alone (Kärcher & Haag, 2004). A possible cutoff of cloud-free ISSs at $s > 0$ is a function of local ice nucleation activity (Haag et al., 2003; Heymsfield et al., 1998).

ISSs extend to negative s-values in the presence of cloud ice, because ice crystals do not sublimate instantly. Exactly how much measured distributions extend to values $s < 0$ depends on how cloud boundaries are defined, that is, when ice crystals become invisible to sensors used to probe cloud particles (Ström et al., 2003).

We present in-cloud ISSs from airborne field campaigns in the midlatitude upper troposphere (MUT) and tropical tropopause layer (TTL). The springtime MUT data were taken during the Mid-latitude Airborne Cirrus Properties Experiment (MACPEX) over the central USA The wintertime TTL data were taken during the Airborne Tropical Tropopause Experiment (ATTREX) over the Pacific. All records have 1 Hz resolution and are mostly tropospheric. Here, a data point is considered to be cloudy if the measured cirrus ice crystal number concentration (ICNC) was above the instrumental detection limit ($\approx$15 L^{-1}) (Thornberry et al., 2017). To better compare the data with our simulation results which consider only small variations around the mean temperature, T_0, we show MUT ($T_0 = 220$ K) and TTL ($T_0 = 190$ K) data selected within the respective temperature windows $T_0 \pm 2.5$ K.

Figure 1 shows ISSs from derived from the MACPEX and ATTREX data sets. Both take their maxima near ice saturation (Krämer et al., 2009), reflecting the effect of cloud ice growth and sublimation on the water vapor concentration in the gas phase. Moreover, they extend to high s-values, arguably capturing homogeneously formed ice crystals right after their formation. The highest positive s-values are associated with the lowest temperatures that appear in the ensemble. In-cloud data points touching the homogeneous freezing thresholds, $s \approx 0.5$ (0.7) in the MUT (TTL), are hard to capture in aircraft measurements due to the short time scales of homogeneous freezing events and rapid growth rates of freshly nucleated ice crystals (Jensen et al., 2022). The higher frequency of occurrence of large supersaturation in the TTL case may be caused by differences in the dynamical forcing or the capacity of cirrus to take up H_2O. We examine the impact of these processes in Section 6.

In the MUT case, the in-cloud statistic derived from the MACPEX measurements is broader in the region $s < 0$ than the simulated ISS, which may point to the lack of very large ice crystals in the simulations. Sufficiently large crystals in fall streaks may stay in dry conditions until they sublimate completely (Hall & Pruppacher, 1976). In the TTL case, the ATTREX distribution increases below about $s = -0.4$ due to sampling of volcanic ash particles in the lowermost stratosphere from the Mount Kelud volcanic eruption (Jensen, Woods, et al., 2018). The injected ash particles were large enough to be detected by the cloud particle probe and are thus mistaken as ice crystals.

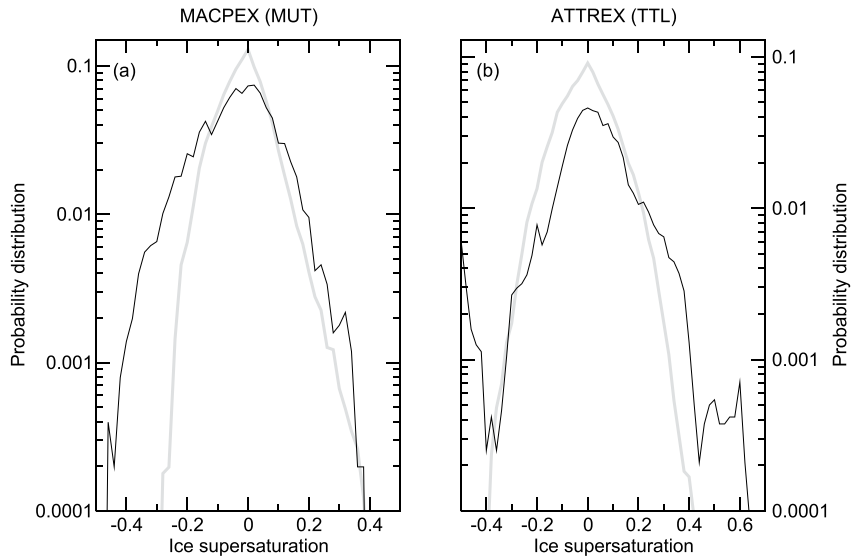

Figure 1. Probability distributions of in-cloud ice supersaturation in the (a) midlatitude upper troposphere (MUT) and (b) tropical tropopause layer (TTL) derived from aircraft observations MACPEX and ATTREX, respectively. The gray curves show baseline results of simulated distributions.

The numerical simulations are driven by GW forcing and assume typical cirrus parameters and maximum ice growth efficiency (deposition coefficient of unity). While the simulations are not intended to provide best fits, the comparison does indicate that the simulations capture the most prominent features seen in the observed ISSs, that is, maxima around ice saturation and the existence of (highly) sub- and supersaturated states. The simulated ISSs exhibit sharper maxima, because all simulations in the ensemble were initialized at ice saturation. We refer to Section 6 for further discussion of simulation results and comparison with the measurements.

3. Methods

We derive the model equations for ice crystal growth by vapor deposition in Section 3.1, describe the stochastic wave forcing driving the evolution of ice supersaturation in Section 3.2, and introduce the parametric approach to determine deposition coefficients in Section 3.3. Air temperature and pressure are denoted by T and p, respectively. The subscript 0 denotes an initial condition.

3.1. Microphysical Model

We derive a set of equations describing the temporal evolution of water phase changes between vapor and cloud ice under the action of vertical air motions. Throughout this work, we approximate cirrus ice crystals by spheres with volume-equivalent radius, r. This approximation is justified, as we are concerned with the effect of bulk partitioning of water mass between the two phases. We avoid the simulation of ice nucleation by prescribing pre-existing ice crystal size distributions based on aircraft measurements, representing a variety of cirrus types, or regions within single cirrus clouds, in different temperature regimes.

We define a discretized cirrus particle number-size distribution (PSD) as a set of number mixing ratios, $\eta_j = \eta(r_j)$, for ice crystals with radius r_j ($j = 1, \ldots, J$). These mixing ratios are linked to ICNCs, n_j, via $\eta_j = n_j/\varrho$, where ϱ is the mass density of air (computed without the moisture contribution). To this end, we prescribe an initial monomodal Gamma distribution (Abramowitz & Stegun, 1972) that has been widely used to parameterize experimental data (Jackson et al., 2015; Mascio et al., 2020):

$$F_r = \frac{\lambda^{\mu+1}}{\Gamma(\mu+1)} r^{\mu} \exp(-\lambda r), \tag{1}$$

with the Gamma function, Γ. The Gamma distribution is normalized to unity and characterized by the scale parameter, λ, and the shape parameter, μ. Cirrus PSDs follow from multiplying F_r with the total ICNC, n. Simulated PSDs evolve over time and may deviate from Equation 1.

The mean number radius (first moment) of F_r is given by $\bar{r} = (\mu + 1)/\lambda$. For the purpose of converting measurement-based mean volume radii (third moment), $\bar{r}_V$, to $\bar{r}$, we note that both are connected via

$$\bar{r}_V = \left[\frac{(\mu + 3)(\mu + 2)}{(\mu + 1)^2}\right]^{1/3} \bar{r}. \tag{2}$$

Cirrus PSDs are typically dominated by sub-100μm crystals (Jackson et al., 2015). Less abundant larger cirrus crystals increase their size only slowly by way of gas diffusion; the main growth process for such ice crystals is aggregation driven by differential sedimentation. In the upper TTL, in-situ formed, optically thin cirrus clouds predominate and super-100μm ice crystals are very rare (Jensen et al., 2008). Values $\mu < 2$ lead to unrealistically high number concentrations of μm-sized ice crystals and setting $\mu > 3$ produces too sharply peaked distributions. Here, we set $\mu = 3$; examples of PSDs are presented in Section 4.

Cloud ice water mass mixing ratios in each size class are defined via

$$q_j = \rho \eta_j \frac{4\pi}{3}\left(r_j^3 - r_c^3\right), \tag{3}$$

where ρ is the bulk ice mass density and r_c is the radius of insoluble ice crystal cores such that $r_j \geq r_c$. (We set $r_c = 100$ nm $\forall j$ and the core mass density equal to that of bulk ice.) Differentiating q_j with respect to time, t, and inserting the diffusion radial growth law per ice crystal, dr_j/dt (D. Lamb & Verlinde, 2011), yields the set of J equations:

$$\frac{dq_j}{dt} = 4\pi D_j n_j r_j f_{\mathrm{K},j} q_{\mathrm{sat}} s, \tag{4}$$

where $q_{\mathrm{sat}}(T)$ is the water vapor mixing ratio at ice saturation. These equations represent rates of deposition or sublimation of water molecules onto or from ice crystals, respectively, depending on whether ambient ice supersaturation, s, is positive or negative. The latter is given by

$$s = \frac{p_v}{p_{\mathrm{sat}}} - 1, \tag{5}$$

where p_v and $p_{\mathrm{sat}}(T)$ are the partial pressures of water molecules in the gas phase and at ice saturation (Murphy & Koop, 2005), both taken at ambient conditions (i.e., in the far field of the ice crystals). Moreover, $f_{\mathrm{K},j}$ is the size-dependent Kelvin correction and D_j is an effective diffusion coefficient for water molecules in air (D. Lamb & Verlinde, 2011) in which a kinetic correction accounts for the radial distribution of water vapor from the far field to the surface of radius r_j-particles:

$$D_j = D_v\left(\frac{r_j}{r_j + \Delta} + \frac{\ell}{\alpha_j r_j}\right)^{-1}, \tag{6}$$

with the uncorrected gas diffusion coefficient, $D_v(p, T)$; the vapor jump distance, $\Delta(p, T)$, roughly equal to the mean free path of water molecules in air; and the diffusion length, $\ell = 4D_v/\bar{v}_v$, where $\bar{v}_v(T)$ denotes the mean thermal speed of water molecules in the vapor. Deposition coefficients for water vapor uptake on ice crystals, α_j, are specified in Section 3.3. Note that they depend explicitly on s and implicitly on r_j, p, and T due to the presence of air.

The above set of equations determining q_j is coupled to the mass mixing ratio of water molecules in the gas phase, q_v, via

$$\frac{dq_v}{dt} = -\sum_{j=1}^{J} \frac{dq_j}{dt} = -\frac{q_v - q_{\mathrm{sat}}}{t_q}, \tag{7}$$

defining the supersaturation quenching (relaxation) time,

$$t_q = \left(4\pi \sum_{j=1}^{J} D_j n_j r_j\right)^{-1}, \tag{8}$$

that describes how rapidly the vapor-ice system approaches steady-state conditions (dynamic equilibria) or, in the absence of temperature changes, thermodynamic equilibrium. Simultaneously solving Equations 3–8 ensures conservation of total water substance.

The Lagrangian evolution of T in air parcels is forced by vertical wind speeds, w, and thus evolves along the dry adiabatic lapse rate, γ. We run simulations with time-dependent fluctuations, $w'(t)$, caused by mesoscale GWs. In the case of pure wave forcing, the air parcel altitude relative to the initial level is given by $z = \int w' dt$; corresponding damped temperature fluctuations, T', follow from integrating the stochastic differential equation

$$\frac{dT'}{dt} = -\gamma w' - fT', \tag{9}$$

where f is the damping rate. Equation 9 is discussed further in Section 3.2. Since the w' values have a mean of zero when averaged over sufficiently long time intervals, the air parcel temperature follows from $T = T_0 + T'$, disregarding any larger-scale motion. Finally, p and ϱ follow from the adiabatic relationship, $p \propto T^{3.5}$, and the ideal gas law for dry air, $\varrho \propto p/T$, respectively.

Sedimentation of ice crystals removes moisture from the air parcel and delays supersaturation quenching, both affecting ice crystal size distributions. To account for sedimentation losses, we remove ice crystals from the parcel according to

$$\frac{d\eta_j}{dt} = -\frac{V}{\delta z}\eta_j, \quad \frac{dq_j}{dt} = -\frac{V}{\delta z}q_j, \tag{10}$$

with an ice supersaturated cirrus layer of vertical depth δz and ice crystal terminal fall speeds, V. Note that for a homogeneous ice crystal distribution in the layer, the average distance ice crystals must settle before being removed from the parcel is $\delta z/2$. We calculate V according to the Stokes relation, obtained by balancing gravity with the drag force for spherical particles falling in still air. This overestimates fall speeds of real ice crystals with non-spherical shapes. We refrain from halving δz, as both modifications tend to offset each other.

Sedimentation of a population of cirrus ice crystals cannot be accurately included in a parcel model framework, as it is based on a prescribed settling layer depth. While choosing too large a δz-value results in no effect of sedimentation within a few hours of simulation time, too small values will remove cloud ice unrealistically rapidly from the simulated air parcels. As an intermediate choice, δz is calculated such that after a maximum simulation time, $t_{\max}$, sedimentation has affected the large size tail of the ice crystal size distribution up to the mean number radius (see Section 4). The effect of the parameterized sedimentation process on ISSs is discussed in Appendix A.

Our results are not sensitive to variations in μ, the mass of aerosol core particles, and the functional form of the initial ice crystal PSD. Concerning the latter, we note that airborne in situ measurements of sub-100 μm cirrus ice crystals are challenging (O'Shea et al., 2016). Equation 4 does not include effects of heat transport and ventilation (the latter also applies to the ice crystal fall speeds), since these are minor for low temperatures (<230 K) and small (<100 μm) ice crystals, respectively.

3.2. Vertical Wind Speed Fluctuations

At cirrus levels, air parcels undergo rapid vertical motions due to GWs inducing MTFs. Away from their source regions, these waves cause an ever-present background of high frequency vertical air motion variability. Quasi-Lagrangian balloon measurements motivate the modeling of wave-induced vertical wind speeds, w', by stochastic time series (Podglajen et al., 2016).

Probability distributions of w' are well approximated by double-sided exponentials with an associated standard deviation, σ_w, from which we draw individual values in the autocorrelated time series, $w'(t)$, used in Equation 9. The autocorrelation time is given by $t_a = 2/\mathrm{N}$ (N is the Brunt-Väisälä frequency) (Kärcher & Podglajen, 2019) and is responsible for the high frequency variability in w' and, hence, in MTFs. The wave-induced vertical

wind speed fluctuations thus change their magnitude and possibly sign every few minutes and have a zero mean value. The correlation time may not be negligible compared to characteristic times scales of ice microphysical processes.

Our stochastic model leads to MTFs that are normally distributed. Non-Gaussian MTF-distributions do occur in nature, albeit infrequently, due to fluctuation intermittency or large-amplitude mountain waves (Bacmeister et al., 1999; Podglajen et al., 2016) or nearby deep convection (Alexander & Pfister, 1995; Corcos et al., 2021). Balloon observations detect non-Gaussian MTFs more frequently in the polar regions than in the tropics (Podglajen et al., 2016). In any case, our methodology is appropriate in conditions away from such strong GW perturbations. For instance, if MTFs arise from deep convection, MTF variance levels off to such background conditions at about 300 km distance to the convective source, depending on wave frequency (Corcos et al., 2021).

Most of the long-duration balloon measurements of vertical wind speed fluctuations were performed in the lower stratosphere. The magnitudes of associated Lagrangian MTFs do not vary significantly across the tropopause (Kärcher & Podglajen, 2019). This allows us to apply the balloon data at lower (cirrus) altitudes.

Sustained random w-fluctuations cause the MTF variance to increase over time. In order for the variance to become asymptotically stationary, MTFs must be damped. This is achieved by Newtonian relaxation, $-fT'$, in Equation 9, where f is the inertial (Coriolis) frequency (Kärcher & Podglajen, 2019). The temperature variance averaged over an ensemble of stochastic $w'(t)$-trajectories approaches a stationary value after 2–3 characteristic MTF damping times, $t_d = 1/f$.

3.3. Deposition Coefficients

We allow variable deposition coefficients, α, by considering a parametric model that is capable of representing major ice crystal growth modes (Nelson & Baker, 1996). This model parameterizes the surface diffusion of water molecules on ice crystal surfaces to attachment sites that promote incorporation into the lattice.

Deposition coefficients take their maximum value, $\alpha = 1$, only if water molecules that strike the surface are instantly incorporated into the crystal lattice (maximum growth efficiency). For molecularly rough surfaces, we expect $\alpha \to 1$. Once facets appear, uptake must be limited and we expect $\alpha < 1$ across crystal facets (Libbrecht, 2005). Vapor growth is then described by different deposition coefficients for each facet.

The development of substantial aspect ratios requires small ice crystals to transition from isometric growth by dislocations (originating from defects in the crystal lattice that appear after ice formation) to growth by the nucleation of steps (Frank, 1982). Both, dislocation growth and step nucleation are associated with faceted growth. Step nucleation is thought to generally occur near the edges and corners of crystal facets. Dislocation growth is still associated with facets, but they produce a larger number of continually growing steps on the surface.

In our simulations, we employ single deposition coefficients, α_j, for ice crystals in each size category. As the model ice crystals are spherical, the deposition coefficients may be viewed as surface-averaged values representing real ice crystals. While this approach does not allow habit evolution, it captures much of the mass growth of small ice crystals at cirrus temperatures (Harrington et al., 2021).

We specify α_j as a function of a critical supersaturation, $s_{\rm crit}(T)$, a parameter selecting a specific growth mechanism, m, and the local ice supersaturation directly above the ice crystal surface, $s_{{\rm sfc},j}$, via the transcendental equation:

$$\alpha_j = \left(\frac{s_{{\rm sfc},j}}{s_{\rm crit}}\right)^m \tanh\left[\left(\frac{s_{\rm crit}}{s_{{\rm sfc},j}}\right)^m\right], \tag{11}$$

which is solved by iteration using the bisection method. The ice supersaturation at the ice crystal surface to be used in Equation 11 is given by

$$s_{{\rm sfc},j} = s\left(1 + \frac{\alpha_j r_j}{\ell}\right)^{-1} \tag{12}$$

(D. Lamb & Verlinde, 2011), implying that the surface supersaturation may differ greatly from that in the ambient air. The critical ice supersaturation defines the boundary between efficient and inefficient growth and m controls

over which range of s-values this transition occurs. Here, we parameterize $s_{crit}(T)$ as a function of supercooling, $\Delta T = 273.15 - T$ [K], in the form

$$s_{crit}\,[\%] = 0.019655 \cdot (\Delta T\,[\mathrm{K}])^{1.4305}, \tag{13}$$

based on the analysis of Zhang and Harrington (2014). In that work, an $s_{crit}(T)$-formulation consistent with Equation 11 was determined by fitting the growth data of Libbrecht (2003). Zhang and Harrington (2014) found that this fit also matched the data from Nelson and Knight (1998) at higher temperatures. Since we simulate isometric ice crystals in the present work, a power-law fit to the average s_{crit}-values of Zhang and Harrington (2014) is used. It is important to note that Equation 13 is strictly valid only for $T > 233$ K, though we extrapolate this parameterization to lower temperatures. The fit gives lower values than the parameterization of Harrington et al. (2019) and therefore provides an upper estimate of the deposition coefficient.

Growth by spiral dislocations, at stacking faults produced during ice formation, and by step nucleation is represented by m-values of 1, 3–5, and >10, respectively. We specify two values, $m = 1$ and $m = 15$. In the case of dislocation growth, α_j-values diminish gradually with decreasing s. In the case of step nucleation, s_{crit} basically acts like a sharp surface supersaturation threshold below which deposition growth is hindered ($\alpha_j \ll 0.1$).

Early facet development on small ice crystals is controlled by dislocations (Nelson & Knight, 1998; Nelson & Swanson, 2019; Pokrifka et al., 2023). The frequent hollowing of ice crystals found across a wide range of temperatures indicates that step nucleation often drives the growth of larger crystals (Wood et al., 2001). On the basis of laboratory experiments, Pokrifka et al. (2020) suggested that ice crystals transition from dislocation to step nucleation as they grow larger and developed a simple method that allows a transition between them, showing that initial growth is more efficient than later growth. This model is also applied here to mimic the transition (dislocation to step nucleation) growth regime. While any morphological changes in ice crystal habits are neglected, this implicitly assumes that facets develop quickly (Gonda & Yamazaki, 1978).

Within the spherical assumption, the transition growth regime is characterized by a size-dependent growth parameter, m_j,

$$m_j = \begin{cases} 1 & : \quad r_j < r_- \\ 1 + 14\left(\frac{r_j - r_-}{r_+ - r_-}\right) & : \quad r_- \le r_j \le r_+ \\ 15 & : \quad r_j > r_+ \end{cases}, \tag{14}$$

with lower and upper limit radii $r_- = 10$ μm and $r_+ = 70$ μm, so that ice crystals enter the step nucleation growth regime ($m > 10$) at $r_j \simeq 50$ μm. In this form, Equation 14 represents results from laboratory measurements of ice mass growth (Pokrifka et al., 2020) and includes the above limiting cases of pure dislocation or pure step nucleation growth.

Surface kinetic resistance appears to be lacking for sublimation, so that sublimation is well described with $\alpha_j(s < 0) = 1$ (Nelson & Knight, 1998; N. B. Magee et al., 2014). This choice is based on observations of rounding of ice crystal facets during sublimation. Rounding indicates true roughening (on the nanometer scale) of the crystal interface. For some simulations, we use this limiting value also to maximize the growth of cloud ice mass, that is, $\alpha_j(s > 0) = 1$.

4. Simulation Scenarios

We carry out all simulations for conditions characterizing the MUT (30°–60° latitude) and the TTL (<30° latitude). These regions are well separated in terms of ambient conditions and cirrus microphysical properties. Regarding temperature and moisture levels, high latitude cirrus (>60° latitude) may be viewed as an intermediate cloud type evolving at conditions midway between TTL and MUT cirrus. Moreover, the altitude of tropical anvil cirrus centers around 200 hPa, and may thus be viewed similar to midlatitude cirrus.

Since conditions in the MUT and TTL scenarios are distinct, different values must be assigned for a number of variables (Table 1). These values are presented as val1 (val2) in their respective units, where val1 is for the MUT and val2 in brackets is for the TTL. As initial conditions, we use $p_0 = 250$ (100) hPa and $T_0 = 220$ (195) K. We

Table 1
Values of Model Parameters Used in the MUT and TTL Scenarios

Scenario	p_0 [hPa]	T_0 [K]	n [L^{-1}]	$\bar{r}$ [μm]	δz [m]	t_a [min]	t_d [h]	t_q [h]
MUT	250	220	5, 50, 500	11, 17, 28	725	2.2	2.5	7, 0.5, 0.03
TTL	100	195	1, 10, 100	4, 10, 15	280	1.1	7.6	50, 2, 0.13

Note. Initial air pressure, p_0, and temperature, T_0; total cirrus ICNCs, n, and number mean ice crystal radii, $\bar{r}$, given as 10-, 50-, 90-percentiles of measurement data representing thin, median, thick cirrus, respectively; sedimentation layer depth, δz; w'-autocorrelation time, t_a, and MTF damping time, t_d; and initial ice supersaturation quenching time for pure gas diffusion, t_q, taken at the integral radii, $n\bar{r}$. Ice crystals are initialized with Gamma number-size distributions with fixed shape parameter, $\mu = 3$, and $J = 100$ size classes. The radius of aerosol core particles in ice crystals is $r_c = 100$ nm. Particle-averaged deposition coefficients for water vapor uptake on ice crystals are either fixed or simulated based on models representing different growth modes or the transition between them. An ensemble contains 500 simulations, each carried out with a time step of 1 s, based on different histories of Lagrangian vertical wind speed fluctuations sampled from an exponential distribution. We distinguish between weak, average, and strong GW forcing regimes and apply ice growth models describing pure dislocation or step nucleation growth, or transition growth. The total runtime for each simulation is limited to 5 hr, but may be smaller depending on sublimation and sedimentation losses.

also define initial cirrus parameters, n and $\bar{r}$. Guided by a comprehensive set of in-situ measurements (Krämer et al., 2020), we identify measured median values with cirrus parameters: $n = 50$ (10) L^{-1}, $\bar{r}_V = 30$ (14) μm. The measurements detected only ice crystals with diameters exceeding 3 μm. Moreover, we adopt the measured 10- and 90-percentiles as representative minimum and maximum values, representing thin and thick cirrus, respectively. We obtain $n = 5$ (1) L^{-1}, $\bar{r}_V = 20$ (7) μm for thin cirrus and $n = 500$ (100) L^{-1}, $\bar{r}_V = 50$ (27) μ m for thick cirrus. For that purpose, we convert the measured mean volume radii, $\bar{r}_V$, to mean number radii, $\bar{r}$ (Section 3.1).

Integral radii $n\bar{r}$ are given by 55 (4) μmL^{-1} for thin, $n\bar{r} = 850$ (100) μmL^{-1} for median, and $n\bar{r} = 14000$ (1500) μmL^{-1} for thick cirrus. The initial quenching time for pure gas diffusion sets an approximate lower limit to values of t_q simulated during cirrus evolution. Supersaturation quenching times are generally substantially longer in TTL cirrus than in MUT cirrus (Krämer et al., 2009). This is brought about by a lower water vapor diffusivity and smaller integral radii in the TTL, see Equation 8. Radial deposition growth rates of individual ice crystals are smaller in cold TTL cirrus due to much lower ice saturation vapor pressures.

We point out that the values for thin and median TTL cirrus in the data set are on the low side of values measured in the TTL. ICNCs of only 1 L^{-1} may be present locally, but hardly define a cloud. They are expected to exert very little impact on ice supersaturation. We recall that the attributes thin, median, and thick may characterize regions within cirrus, not only entire clouds.

The sedimentation layer depth is estimated from $\delta z = Vt_{\max}$ at $\bar{r}$ (median values) and T_0. With fall speeds $V \approx 4$ (1.5) cm s^{-1} and $t_{\max} = 5$ hr (see below), this yields $\delta z \approx 725$ (280) m. Sedimentation losses are smaller (larger) for thin (thick) cirrus.

To study the effect of different vertical wind speed levels, we employ a range of values, $\sigma_w = 0.05$–0.25 m s^{-1} (Kärcher & Podglajen, 2019), defining very weak to very strong GW forcing regimes. Increasing (decreasing) σ_w increases (decreases) the relative frequency of occurrence of strong up- and downdrafts ($|w'| > 1$ m s^{-1}). Brunt-Väisälä and Coriolis frequencies are chosen such that for $\sigma_w = 0.15$ m s^{-1} the asymptotic (damped) MTF standard deviation averaged over all trajectories in an ensemble is 1.15 (1.43) K for the MUT (TTL) for average forcing (Section 3.2).

A baseline simulation is defined by average GW forcing ($\sigma_w = 0.15$ m s^{-1}) and median cirrus. We recall from Section 3.3 that we calculate deposition coefficients for dislocation and step nucleation growth separately and compare the results with a model that parameterizes the transition between them. In some simulations, we employ maximum growth efficiency, $\alpha_j(s > 0) = 1$, to minimize the surface kinetic resistance to deposition growth and thus maximize the impact of ice growth. We do not consider possible impacts of ice nucleation on our results, since we prescribe initial ice crystal PSDs in our simulations.

We employ $J = 100$ radial classes to represent and track cirrus ice crystal PSDs. Associated initial r_j-values increase progressively from 1 μm to $3\bar{r}$. Ice crystals in each class grow or sublimate to their exact sizes. During growth (sublimation), ice crystals deposit (release) water vapor, thereby inducing a tendency to restore ice

Table 2
Description of Numerical Simulations

Simulation	Characteristics	Assumptions	Section
Idealized	Quenching phase	No forcing	5.1
Idealized	Weak forcing trajectory	Constant updraft	5.2
Idealized	Single stochastic trajectory	Baseline + max. growth eff.	5.3
Ensemble	Trajectory ensemble	Baseline + max. growth eff.	6.1
Ensemble	Cirrus thickness (n, $\bar{r}$ variations)	Maximum growth efficiency	6.2
Ensemble	Vertical wind speed (σ_w variation)	Maximum growth efficiency	6.3
Ensemble	Variable deposition coefficients	Baseline	6.4

Note. Baseline simulations employ average stochastic GW forcing ($\sigma_w = 0.15$ m s^{-1}) and median cirrus parameters (Table 1). Maximum growth efficiency assumes that all deposition coefficients are unity, thus maximizing the impact of ice growth.

saturation. Class-j ice crystals sublimate until $q_j = 0$ is reached, at which point they are removed from the distribution by setting $\eta_j = 0$. If $s < 0$ occurs often or long enough, the whole cloud may eventually dissipate. Sedimentation has a similar effect, but acts on longer time scales.

Table 2 summarizes all simulation cases discussed in this study along with their underlying assumptions. More complexity is added successively to the simulations, which range from an idealized scenario with no forcing of supersaturation to ensemble simulations with GW forcing.

We first present results from idealized simulations assuming vanishing or constant updraft speed. In view of the random walk nature of air parcel trajectories, we then perform a large number of more realistic simulations with stochastic vertical wind forcing and derive probability distributions (ISSs). To generate robust statistics, we calculate 500 representations of each distribution based on different temporal w'-histories, defining one ensemble. The distributions in an ensemble are averaged and their properties analyzed and compared to aircraft measurements.

In each stochastic cirrus simulation, we choose initially ice-saturated conditions, $s_0 = 0$, without variability in T_0 and q_v; the assumption of mean ice saturation within cirrus is supported by a number of observations (Kärcher et al., 2018; Krämer et al., 2009). We use a resolution in s of 0.02 to build discrete ISSs. The time step in all simulations is set to 1 s. One of two criteria is used to terminate each simulation: (a) all cirrus ice crystals are fully sublimated, thus, $\sum_j \eta_j = 0$; (b) the vertical distance exceeds $\pm$ 500 m away from the initial location. This ensures that only in-cloud conditions are sampled and unrealistically large air parcel lifting or sinking distances are avoided. If these criteria are not met, a simulation is terminated when its total runtime, t_{max}, exceeds 5 hr, since the air parcel framework becomes increasingly unrealistic with time. Average simulation times vary depending on sublimation and sedimentation losses.

In sum, our study combines stochastic ensemble simulations with an advanced, physically-based treatment of cirrus dynamical forcing and kinetic ice crystal growth processes based on the latest findings from field and laboratory measurements. By contrast, the analysis of Zhao and Shi (2023) was based on a single cirrus forcing and thermodynamic regime without accounting for the basic fact that ice deposition coefficients vary with ambient conditions and by employing constant low values of the deposition coefficient also for the sublimation process, both unsupported by experimental evidence.

5. Idealized Simulations

We start by investigating results from idealized scenarios that focus on pure ice crystal growth and sedimentation during the supersaturation quenching phase (Section 5.1) and in a slow constant updraft (Section 5.2). While both scenarios are clearly not realized over a cloud's lifetime in the atmosphere, they help interpret results from simulations with stochastic forcing and allow us to gain first insights into the importance of kinetic limitations to cirrus ice production for given forcing and cirrus parameters. We compare results based on transition growth with supersaturation-dependent deposition coefficients (Section 3.3) with those based on a deposition coefficient of unity in each case, representing the weakest possible kinetic limitation to deposition growth. The impact of stochastic forcing along a single trajectory (Section 5.3) is based on maximum growth efficiency.

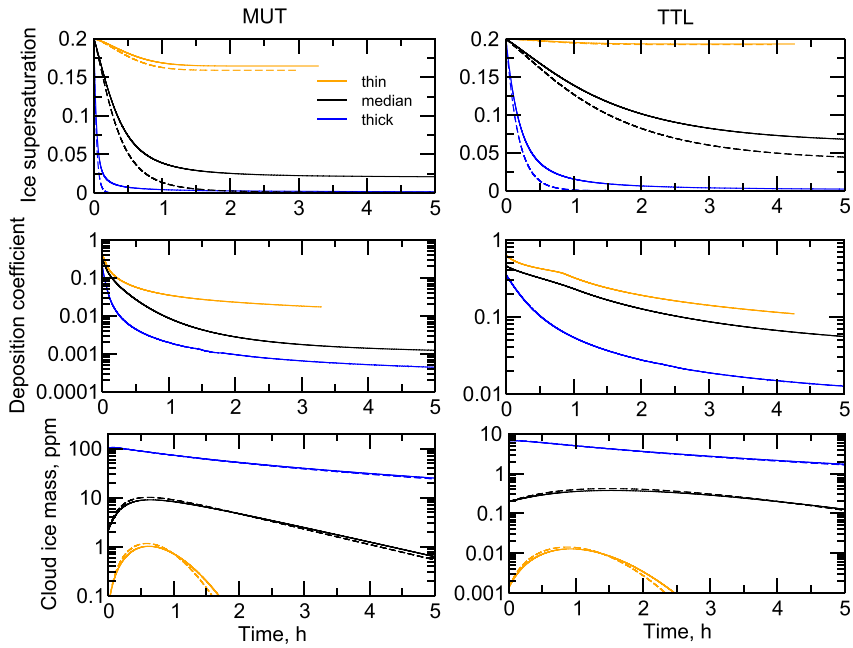

Figure 2. No forcing scenario (Table 2). Time series of (top panel) ice supersaturation, (mid) deposition coefficient averaged over the cirrus ice crystal size distribution, and (bottom) total cloud ice mass mixing ratio for the (left panel) MUT and (right) TTL case without dynamical forcing and variable deposition coefficients calculated for transition growth. Shown are results as solid curves for thin, median, and thick cirrus. The corresponding dashed curves in the top and bottom panels are based on maximum growth efficiency.

5.1. No Forcing

To study the supersaturation quenching phase, we set the vertical wind speed to zero and initialize each simulation for different cirrus parameters with a moderate ice supersaturation ($s_0 = 0.2$).

Figure 2 confirms that supersaturation quenching times are very long for thin cirrus in general and even for median TTL cirrus (Table 1). Moreover, cloud ice mass decreases after initial uptake of a large amount of water vapor. This implies that the lifetime of all cirrus in such a scenario is eventually limited by sedimentation. This limitation is apparent only for thin cirrus with relatively low ICNCs. Thin cirrus vanish within 3 hr due to the large sizes obtained during growth in this time, around 70 μm in the MUT and 20 μm in the TTL.

As ice crystal size increases, the supersaturation near the crystal surface declines and this causes a decrease in the deposition coefficient. In the MUT, early growth takes place efficiently in the dislocation mode and the last stages of growth occur in the less efficient step nucleation growth mode. In the TTL, growth does not transition away from the dislocation mode as much as in the MUT due to the smaller mean crystal sizes. Consequently, deposition coefficients there are typically larger than in the MUT. While thick cirrus drive s quickly down to zero in both, MUT and TTL scenarios, sedimentation losses prevent s from relaxing to near ice saturation in the case of thin cirrus, leaving substantial supersaturation behind ($s = 0.16$–0.19).

The effect of variable deposition coefficients is rather small in all cases, as revealed by the comparison with the results based on maximum growth efficiency, suggesting that kinetic limitations to ice growth are weak during supersaturation quenching. In fact, during the initial growth phase, in which the cloud ice mass reaches a maximum value (around 0.5 hr for thin and median, and 0.1 hr for thick cirrus), ice crystal number-averaged deposition coefficients do not decrease significantly below 0.1. In the final growth phases of median and thick cirrus, deposition coefficients decline significantly as crystal sizes increase, but growth rates are small anyway due to small ambient supersaturation.

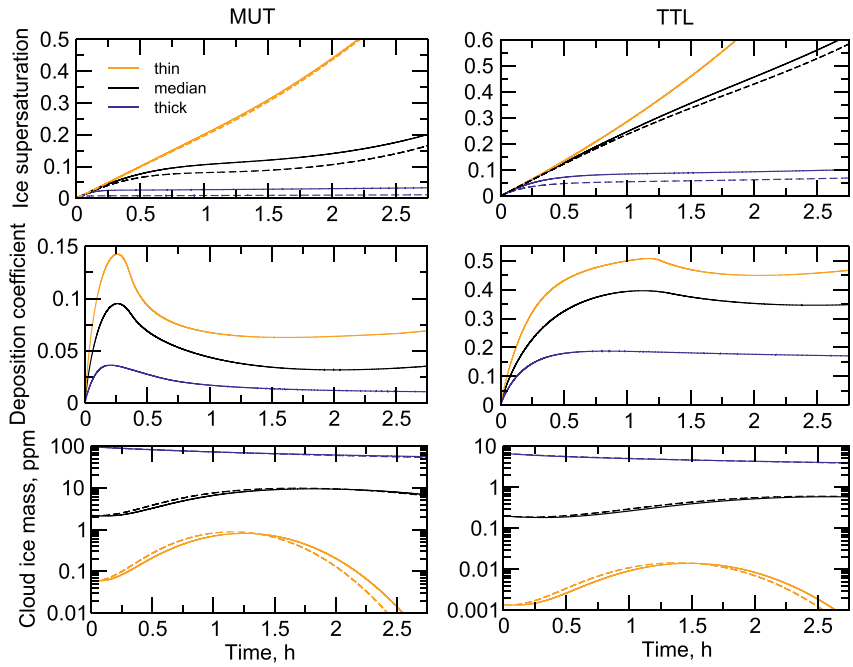

Figure 3. Constant updraft scenario (Table 2). Time series of (top panel) ice supersaturation, (mid) deposition coefficient averaged over the cirrus ice crystal size distribution, and (bottom) total cloud ice mass mixing ratio for the (left panel) MUT and (right) TTL case in a slow updraft (0.05 m s^{-1}) and with variable deposition coefficients calculated for transition growth. Shown are results as solid curves for thin, median, and thick cirrus. The corresponding dashed curves in the top and bottom panels are based on maximum growth efficiency.

5.2. Constant Updraft

To maximize the impact of variable deposition coefficients on ice supersaturation and cirrus ice mass, we prescribe a low updraft speed of 0.05 m s^{-1}. All simulations are initialized at ice saturation and stop after 2.78 hr when the air parcel lifting distance reached 500 m.

Figure 3 shows that the evolution of ice supersaturation is determined by the imposed slow cooling (source term) and uptake on the pre-existing cloud ice crystals (loss term). For thin cirrus, deposition losses hardly affect s, which increases toward homogeneous freezing levels. This also true for median TTL cirrus. In thick cirrus, deposition losses dominate and thus keep s close to equilibrium.

Deposition coefficients are initially very small, but quickly rise to values above 0.01 (0.1) in the MUT (TTL). They start to slightly decrease due to the increase in ice crystal sizes, an effect that is more pronounced in the MUT as the larger cirrus particles grow farther into the step nucleation growth regime. As in the no forcing scenario, the temporal evolution of cloud ice mass is governed by initial growth and later sedimentation. The latter process commences in thin cirrus rather abruptly after ice crystals grow sufficiently large, and acts gradually in thick cirrus with much larger crystals present to begin with.

The effect of variable deposition coefficients is again small. They take very small values only when s is close to zero, in which case there is no driver for vapor growth in the first place, see Equation 12. At later stages, s increases significantly, at which point deposition coefficients are large enough to no longer limit growth. Kinetic effects on cloud ice mass growth would be smaller at higher updraft speeds, in which case larger supersaturation, hence, larger α_j-values, are reached more quickly.

5.3. Impact of Stochastic Wave Forcing

In the remainder of this work, dynamical forcing is treated more realistically based on high frequency GWs. Here, we show how ice supersaturation, cirrus PSDs, and cloud ice mass change along a single stochastic time series

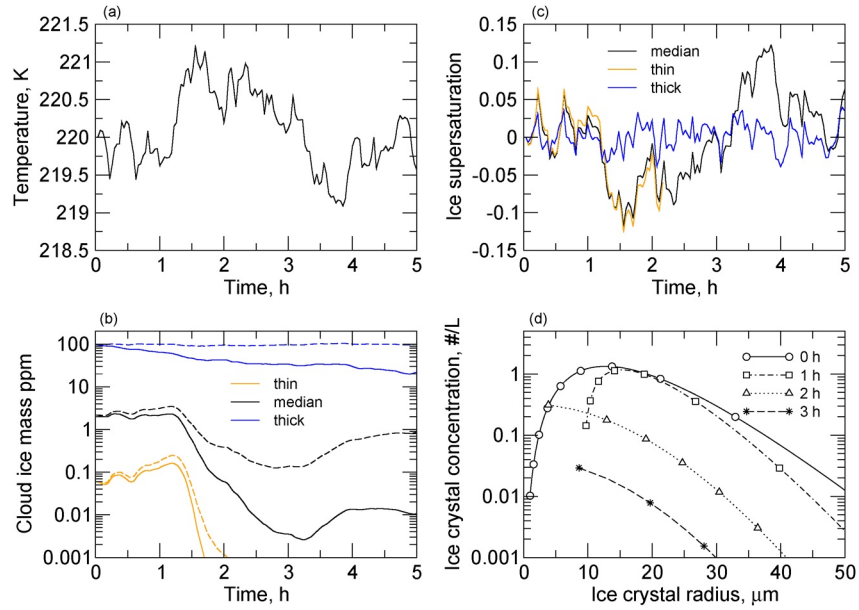

Figure 4. Time series of (a) mesoscale temperature fluctuations, (b) cloud ice mass mixing ratio, (c) in-cloud ice supersaturation, and (d) ice crystal number-size distributions for the MUT scenario, average forcing ($\sigma_w = 0.15$ m s^{-1}), and maximum growth efficiency ($\alpha_j = 1$). The dashed curves in (c) were computed neglecting the effect of sedimentation. The distributions in (d) are shown for median cirrus parameters only. The symbols mark every 10-th (0 hr, 1 hr) and every second (2 hr, 3 hr) out of 100 initial ice crystal classes.

of vertical wind speed perturbations. We restrict this discussion to the baseline MUT case and maximum growth efficiency, for simplicity.

Figure 4 shows selected results, in which MTFs vary within about ±1 K around the mean value $T_0 = 220$ K. After brief cooling phases in the first hour, warming occurs between $t = 1$–2 hr followed by cooling up to about $t = 4$ hr. The cirrus responds to the temperature evolution by increasing and decreasing its cloud ice mass. Sedimentation reduces cloud ice mass significantly for median and thick cirrus. Due to the size spectrum, a number of ice crystals with sizes small enough so that their fall speeds are insignificant, survive. However, they are efficiently removed by sublimation in the transient warming phases. While median and thick cirrus do not dissipate within 5 hours of simulation time, sublimation losses are large enough to eliminate all ice crystals in thin cirrus, limiting its lifetime to about 2.5 hr in this case.

We note in passing that toward the end of its life cycle, ICNCs might be low enough to allow new ice formation in cloudy areas during further cooling phases. This process is not included here.

The supersaturation in thin cirrus approximately mirrors the MTFs, that is, conditions close to the cloud-free situation. However, *s*-amplitudes slightly decrease for median cirrus due to the damping effect of cloud ice, but the temporal evolution is still mainly governed by the stochastic GW forcing. By contrast, cloud ice growth in thick cirrus is strong enough to constrain supersaturation to lie within a few percent around ice saturation.

The temporal evolution of the PSDs for median MUT cirrus is correlated with that of cloud ice mass and *s*. After 1 hr, the smallest crystals in initial spectrum have grown to larger radii (≥10 μm), as diffusional growth rates are larger for smaller crystals. At the same time, sedimentation has begun to act on the larger (>30 μm) ice crystals in the spectrum. The warming between $t = 1$–2 hr has a marked impact on the PSD: all ice crystals below about 5 μm are lost from the cirrus, and the total ICNC (not shown) decreased significantly. This situation continues up to about $t = 4$ hr, and later only few crystals with radii in the range 10–30 μm remain. The fact that MTFs tend to sublimate small cirrus ice crystals in the warm phases may explain why the numerous small ice crystals generated by homogeneous freezing in TTL cirrus do not seem to persist (Jensen et al., 2022).

Clearly, compared to idealized simulations based on constant updrafts, the GW forcing of ice supersaturation results in a more realistic evolution of cirrus clouds. In particular, stochastic cooling and warming phases act to

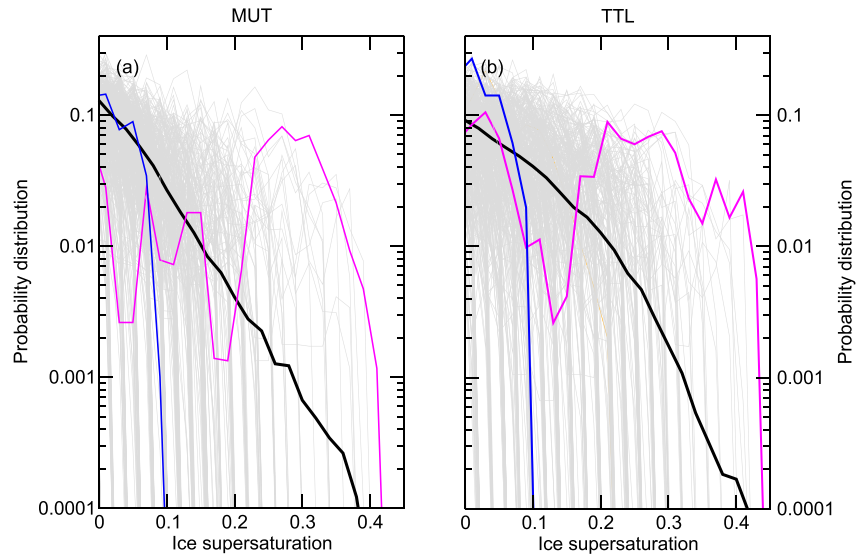

Figure 5. Probability distributions of in-cloud ice supersaturation in the (a) MUT and (b) TTL from baseline simulations with maximum growth efficiency. The gray thin curves in each case represent the full ensemble of simulated ISSs discretized over the supersaturation grid. The black curves show the corresponding ISSs averaged over the ensemble. The blue and magenta curves mark ISSs close to ice saturation and those containing the highest supersaturation values, respectively.

extend cirrus lifetimes compared to a constant, slow updraft scenario (Corcos et al., 2023). In our specific case, a small range of ice crystal radii around 20 μm happens to be a sweet spot in the MUT PSD that is neither significantly affected by sublimation nor by sedimentation over 3 hr of simulation time.

6. Ensemble Simulations

We present and systematically analyze results from ensemble simulations that consider stochastic GW forcing of the vertical wind field and compare them with the aircraft measurements introduced in Section 2. We only compare ensemble-mean ISSs with the measurements, as the aircraft data cover a wide range of vertical wind speeds and cirrus parameters. We focus on the parts of ISSs where ice clouds persist ($s \geq 0$). We use maximum deposition coefficients for all ice crystals, $\alpha_j = 1$, to illustrate the full range of ISSs present in an ensemble (Section 6.1) and to study effects of cirrus thickness (Section 6.2) and vertical wind speeds (Section 6.3), before studying the role of different models for the deposition coefficient (Section 6.4).

6.1. Supersaturation Variability Along Trajectory Ensembles

Figure 5 shows the tremendous variability in the ISSs along each of the 500 individual time series of stochastic vertical wind speed fluctuations in both the MUT and TTL scenario. The ensemble simulations are based on average forcing ($\sigma_w = 15$ cm s^{-1}), median cirrus parameters, and maximum deposition coefficients ($\alpha_j = 1$).

The simulated ensemble-mean ISSs replicate the main features seen in measured ISSs (Section 2). The blue curves mark one out of many individual ISSs close to thermodynamic equilibrium $s < 0.1$) along trajectories with only weak to moderate updrafts. By contrast, either a sequence of strong updrafts or significantly reduced ICNCs (due mainly to sublimation) or a combination of both lead to pronounced yet much rarer transient non-equilibrium states, as illustrated by the secondary maxima in the range $s = 0.2$–0.4 in the magenta curves. Cloud ice growth counteracts the build-up of such states. In this baseline case, the presence of cloud ice prevents homogeneous freezing (that would set in above $s \approx 0.5$).

We note the clustering of individual ISSs around ice saturation up to about $s = 0.15$ (0.25) in the MUT (TTL) and the large spread of trajectories into the highly supersaturated regime. Vertical wind speed fluctuations similar to those generated by GWs are thus needed to create such broad maxima. The distribution spread may not be reproduced in simulations based on synoptic-scale updrafts, depending on the ratio of lifting and supersaturation

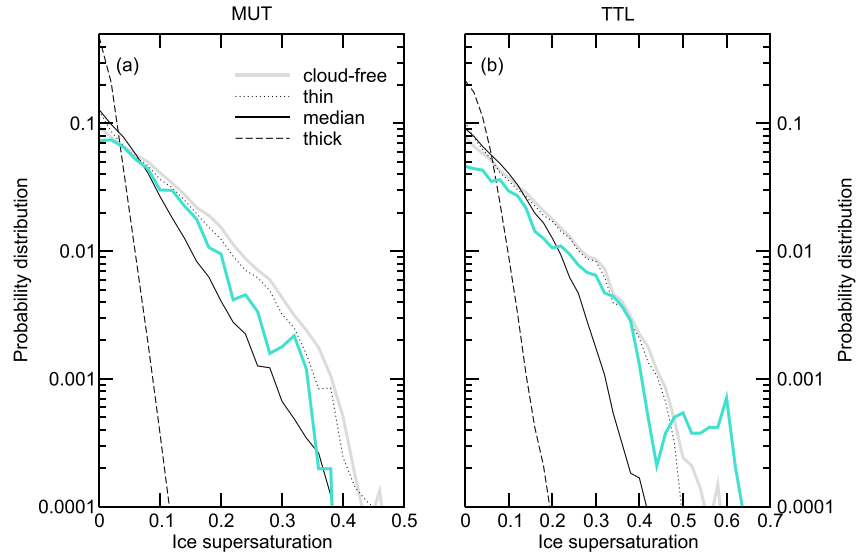

Figure 6. Probability distributions of in-cloud ice supersaturation in the (a) MUT and (b) TTL from numerical simulations based on average forcing and maximum growth efficiency. The dotted, solid, and dashed black curves are computed for thin, median, and thick cirrus, respectively. The gray curves show the corresponding simulated cloud-free statistics as limiting cases. The turquoise curves show the measured in-cloud statistics from Figure 1.

quenching timescales. Arguably, the wide range of local ISS shapes that change on a minute timescale (t_a) plays an important role in the evolution of individual cirrus clouds.

6.2. Effect of Cirrus Thickness

We investigate how ISSs respond to changes of total cirrus ICNCs and mean ice crystal radii, again for average forcing and maximum growth efficiency.

Figure 6 shows the simulated in-cloud ISSs for thin, median, and thick cirrus based on measured 10,50, and 90-percentile cirrus parameters, n and $\bar{r}$ (Section 4). While the stochastic GW forcing acts to broaden supersaturation distributions, the main effect of cloud ice is to dampen supersaturation fluctuations (Kärcher et al., 2014). The thin cirrus distributions are very close to the simulated cloud-free distributions, because the quenching times are too long for ice crystals to strongly interact with the gas phase.

The most obvious feature in both, MUT and TLL scenario is the systematic decrease in distribution width with increasing integral radii, successively eliminating strongly supersaturated states. In particular, the standard deviation decreases from 0.09 (0.12) for thin to 0.08 (0.11) for median, to only 0.02 (0.04) for thick cirrus in the MUT (TTL). For thick MUT cirrus, the statistics are almost symmetric and confined to values up to about ±0.1 around ice saturation.

Measured MTF distributions may show rare, non-Gaussian departures in their wings (Section 3.2), but simulated MTFs are normally distributed. If our model included such large-amplitude temperature perturbations, the simulated distribution wings would be associated with higher probabilities of occurrence. This may improve the comparison with the TTL data above $s = 0.4$. However, changes in the mean temperature also play a role, as deposition and sublimation rates are about an order of magnitude faster in MUT compared to TTL conditions.

While measured in-cloud ISSs are bounded by their simulated cloud-free counterparts, they cut across the simulated in-cloud statistics. This is expected, since the measurements encompass thin, median, and thick cirrus considered in the simulations. While it would be instructive to select measured ISSs for different ranges of integral radii comparable to the simulation cases shown in Figure 6, the limited amount of aircraft data available does not support such a subsetting, as even the ISSs with all data included are noisy.

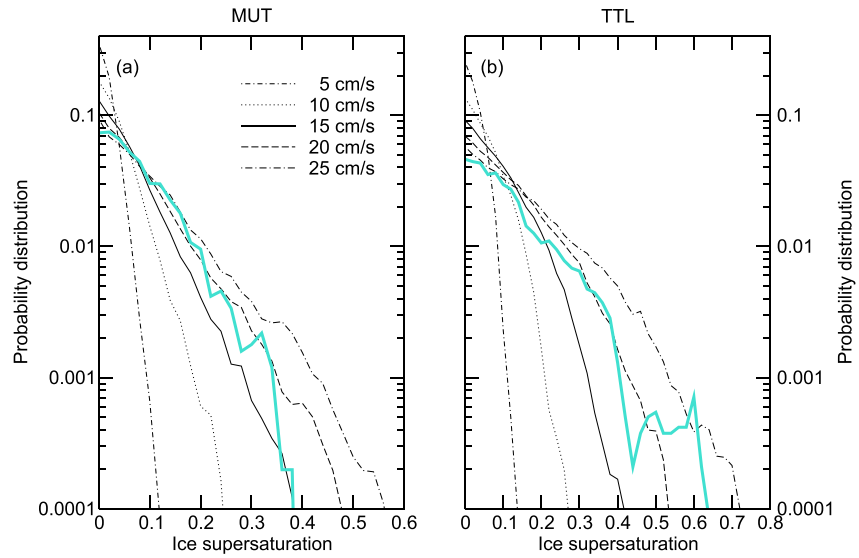

Figure 7. Probability distributions of in-cloud ice supersaturation in the (a) MUT and (b) TTL from numerical simulations based on median cirrus parameters and maximum growth efficiency. Black curves correspond to σ_w-values as indicated in the legend. The turquoise curves show the measured in-cloud statistics from Figure 1.

6.3. Effect of Vertical Wind Speed Variance

We examine how ISSs respond to changes of the assumed average w'-amplitude. We repeat the in-cloud simulations with median cirrus properties with σ_w enhanced and reduced by 5 and 10 cm s^{-1} to bracket a very wide range of dynamical forcing conditions. Also these ensemble simulations assume maximum deposition coefficients.

Figure 7 shows that cloud-scale dynamical forcing has a profound impact on the distribution of in-cloud supersaturation that easily rivals variations induced by large changes in integral radii as discussed above. For $\sigma_w = 15$ cm s^{-1} (average forcing), the lack of highly supersaturated states ($s > 0.4$) reduces, on average, the likelihood of homogeneous ice formation, except in the thinnest cirrus clouds. (We recall that we do not include this process in our simulations.) Homogeneous freezing may still occur on individual subsets of ISSs found in the ensemble (Figure 5).

While low average updraft speeds cause rather narrow distributions, more vigorous forcing may cause ice supersaturation high enough to trigger homogeneous freezing events within cirrus, albeit in only fewer than 1% of all cases for $\sigma_w = 25$ cm s^{-1} in the MUT case. Higher s-values are reached in TTL conditions due to a lower mean temperature in combination with the non-linear T-dependence of p_{sat}.

For comparison, we show the measured in-cloud statistics. They cut across the simulated distributions, since presumably σ_w was variable during the measurements. The sharp drop of the MUT data slightly below $s = 0.4$ might be indicative of heterogeneous ice nucleation. However, given the strong case-to-case variability in ISSs, this is not conclusive. By contrast, the TTL data extend to values of s high enough to induce homogeneous freezing. We note that this does not exclude moderate heterogeneous ice activity, which is currently poorly characterized in the TTL (Jensen, Kärcher, et al., 2018). The dip around $s = 0.5$ in the TTL data may be a statistical abberation in the limited data sample.

6.4. Effect of Deposition Coefficients

We explore how different models for vapor growth affect ISSs, deviating from the assumption of maximum growth efficiency. To begin with, we apply the parametric model Equations 11–13 describing pure dislocation ($m = 1$) and step nucleation growth ($m = 15$), respectively, in baseline simulations (average forcing, median cirrus).

Figure 8 shows that supersaturation-dependent deposition coefficients alter the baseline ISSs by slightly enhancing the frequency of occurrence of ice-supersaturated states. The overall effect is more pronounced

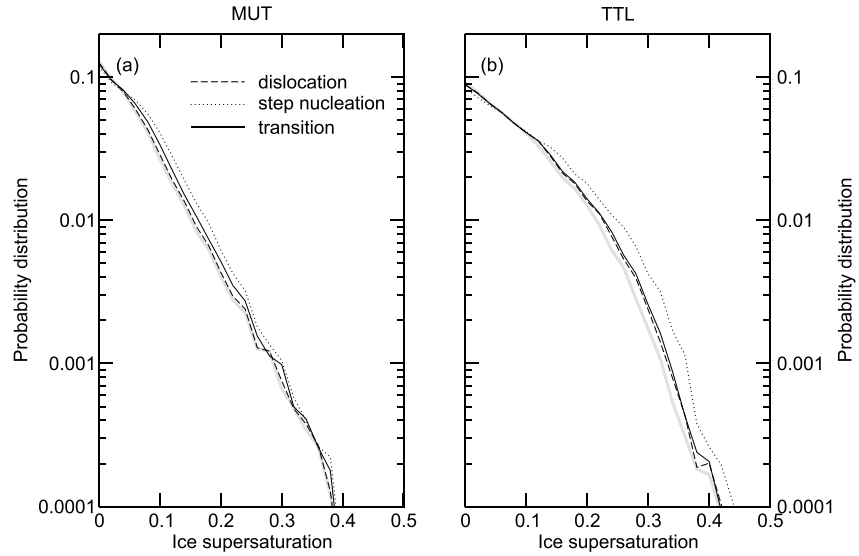

Figure 8. Probability distributions of in-cloud ice supersaturation in the (a) MUT and (b) TTL from baseline simulations with variable deposition coefficients. The solid black curves represent growth in the transition regime. The dotted and dashed curves represent growth by dislocations and step nucleation only, respectively. The gray curves show the same baseline cases with maximum growth efficiency, repeated from Figures 6 and 7 based on average forcing and median cirrus.

for pure step nucleation growth due to the faster decline of α_j-values below the critical ice supersaturation, $s_{\text{crit}}(T)$, which takes values around 0.07 (0.1) in the MUT (TTL) case. For intermediate supersaturation, the effect also happens to be somewhat larger in the TTL, as the low temperatures there generally lead to small growth rates. By design, growth in the transition regime interpolates between these two limiting cases. In the TTL scenario, the transition ISS is very similar to the dislocation growth case due to the small ice crystal sizes.

The results from sensitivity studies in Appendix A suggest that ice crystal sedimentation might exert a larger effect on ISSs than deposition growth assumptions. Addressing this issue in more detailed requires the use of a model with vertical resolution.

The impact of supersaturation-dependent deposition coefficients on ISSs is limited. To better interpret this finding, we inspect the corresponding probability distributions of deposition coefficients with the help of Figure 9. Similar to the ISSs, each curve represents an average over all 500 individual distributions that were taken at every simulation time step and ice crystal size class (excluding excessively small α_j-values that occur very close to ice saturation).

In both the MUT and TTL cases, the general shape of the PDF is caused by the monotonically decreasing number of supersaturated states seen in the ISSs. For transition growth, low and high values of deposition coefficients, corresponding to low and high s-values in the respective ISSs, are bounded by the individual cases, as expected. The broad range of simulated deposition coefficients is brought about by the vast number of dynamically triggered s-values and the large size range of cirrus ice crystals. While values exceeding $s = 0.4$ (0.6) are basically absent in the MUT (TTL) for average forcing and median cirrus, conditions near ice saturation as the most prevalent states in ISSs cause the PDF of deposition coefficients to be negatively skewed. This number is larger for step nucleation growth, as deposition coefficients decline steeply for $s < s_{\text{crit}}$ (Section 3.3).

Most α_j-values for transition growth lie near 0.03 (0.2) in the MUT (TTL). In order for deposition coefficients to limit water vapor uptake, the dimensionless group, $\ell/(\alpha_j r_j)$, in the vapor diffusivity, Equation 6, must exceed unity. Evaluating this term at median $\bar{r}$, T_0, and p_0 shows that values $\alpha_j \ll 0.01$ (0.04) are needed in the MUT (TTL) to impose significant kinetic limitations to diffusional growth. Together with the fact that the wave forcing generates non-equilibrium cirrus states most of the time, thereby reducing the likelihood to find exceedingly low α_j-values that develop close to ice saturation, this explains why the effect of variable deposition coefficients on ensemble average ISSs is rather small.

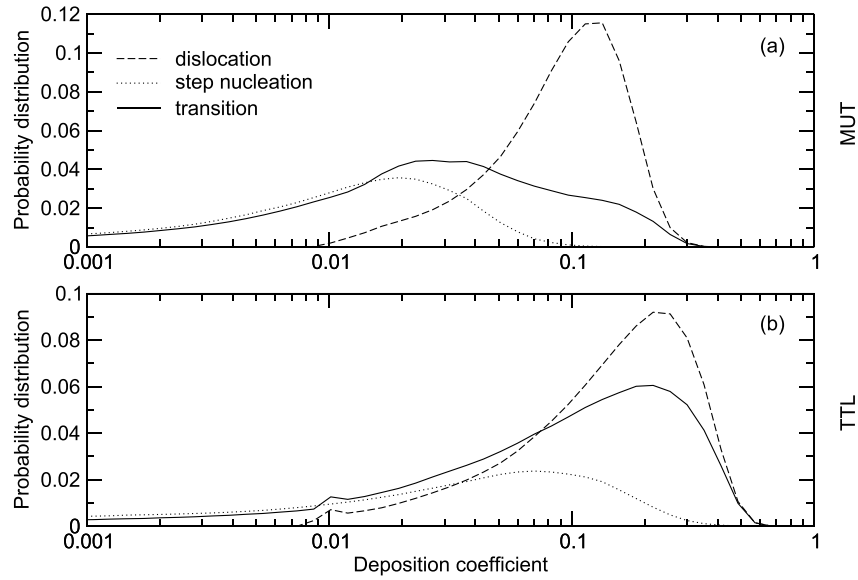

Figure 9. Probability distributions of deposition coefficients in the (a) MUT and (b) TTL from baseline simulations. These distributions correspond to the ISSs shown in Figure 8. The solid curves represent growth in the transition regime. The dashed and dotted curves represent growth by dislocations and step nucleation only, respectively.

With transition growth viewed as the most realistic parameterization, we finally study its impact on ensemble average ISSs for different cirrus (Figure 10) and forcing (Figure 11) regimes. Variable deposition coefficients exert not only a small effect on ensemble average ISSs in baseline conditions, as discussed with the help of Figure 8, but also across a wide range of values for σ_w and $n\bar{r}$. Supersaturation quenching times in cirrus are typically much longer than the autocorrelation time of the vertical wind speed fluctuations (Table 1), except for thick cirrus. This means that GWs typically change the dynamical forcing conditions faster than cloud ice microphysical processes can respond to the resulting changes in supersaturation.

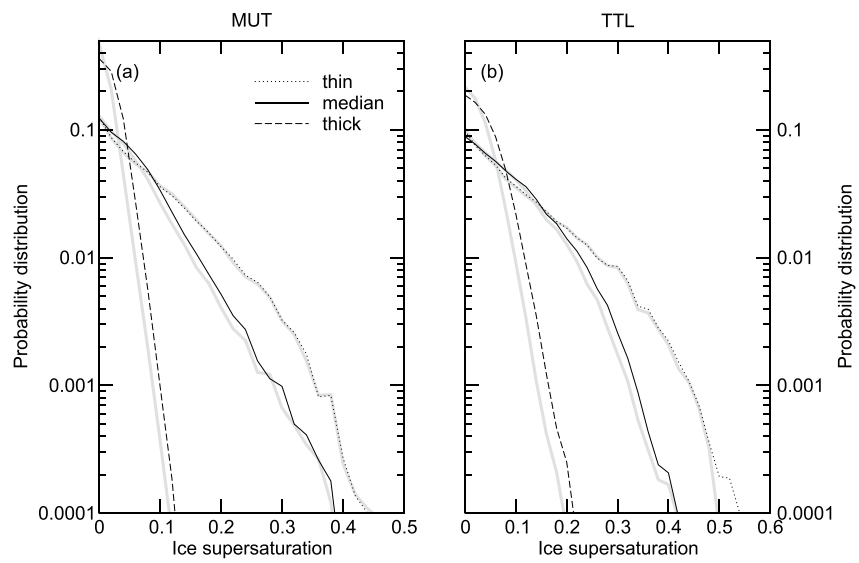

Figure 10. Probability distributions of in-cloud ice supersaturation in the (a) MUT and (b) TTL from numerical simulations based on transition growth and average forcing. Black curves are computed for thin, median, and thick cirrus as indicated in the legend. The gray curves are the corresponding results show from Figure 6 based on maximum growth efficiency.

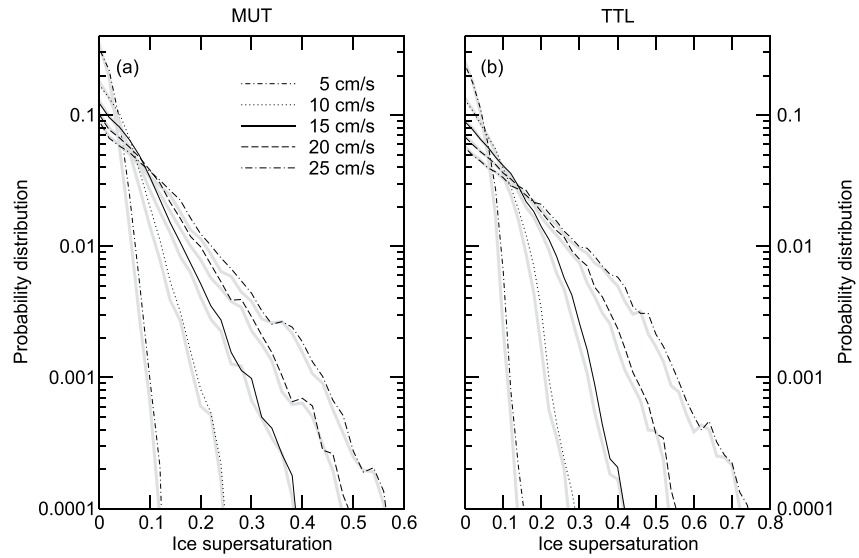

Figure 11. Probability distributions of in-cloud ice supersaturation in the (a) MUT and (b) TTL from numerical simulations based on transition growth and median cirrus. Black curves correspond to σ_w-values as indicated in the legend. The gray curves are the corresponding results repeated from Figure 7 based on maximum growth efficiency.

7. Summary and Conclusions

This work systematically investigated on the process level local dynamical and microphysical factors controlling ISSs within upper tropospheric cirrus clouds. We distinguished between midlatitude and much colder and higher TTL cirrus. We studied how changes in the strength of vertical air motions induced by GWs and water vapor attachment kinetics on ice crystal surfaces affect ISSs in ensemble simulations employing stochastic time series of vertical wind speed fluctuations. We defined regimes of weak, average, and strong forcing of supersaturation in background conditions due to GWs and thin, median, and thick cirrus based on total cirrus ice crystal number concentrations and mean radii. These broad categorizations are based on atmospheric measurements. We also discussed cirrus evolution in idealized simulations that include a case without forcing addressing pure supersaturation quenching and one with a constant updraft speed.

We applied a novel model for ice deposition coefficients as a function of surface supersaturation, temperature, and ice crystal size. This parameterization is derived from laboratory measurements and describes the transition from an initially rough sphere with emerging facets growing efficiently by dislocations to facets growing less efficiently by step nucleation. We presented, for the first time, probability distributions of deposition coefficients in cirrus clouds, showing that previous low values constitute only a small subset and thereby refuting a strong influence of surface-kinetic limitations on ice crystal growth from the vapor in cirrus simulations (Gierens et al., 2003; N. Magee et al., 2006).

7.1. Summary of Results

Midlatitude and tropical tropopause ISSs within cirrus show broad maxima around ice saturation and distribution wings extending to large absolute values of s. ISSs in the TTL have larger variances (extend to higher supersaturation) than in the MUT for the same forcing due to lower air temperatures.

Supersaturation quenching times in cirrus can exceed several hours, causing thin and median cirrus to evolve in distinct non-equilibrium states across much of their life cycle. ISSs in thin cirrus regions are very close to cloud-free distributions that are mainly determined by temperature variability.

Study of ISSs on the process level is meaningful only in relation to local vertical wind speed fluctuations, which induce alternating cooling and warming phases. This causes a remarkably large variability in ISSs and underlying ice cloud microphysical properties due to different representations of these fluctuations along single air parcel trajectories.

Ensemble-mean statistics based on GW forcing exhibit main features of observed ISSs. When taken in thin cirrus, such ISSs exhibit the largest variance and are close to ISSs in cloud-free air in the same forcing conditions. ISS variance decreases notably with increasing integral radius from median to thick cirrus such that statistics taken in thick cirrus are confined to a narrow region around ice saturation.

ISS variance responds strongly to changes in the mean vertical wind speed fluctuation amplitude, as the saturation vapor pressure instantly responds to temperature changes. Ice supersaturation may at times reach values high enough to trigger homogeneous freezing events in areas where ICNCs are sufficiently low. GWs typically change ice supersaturation faster than cloud ice microphysics is capable of responding to by deposition or sublimation. The associated MTFs allows for a more realistic cloud evolution, that is, longer lifetime, compared to situations without MTFs.

GW forcing generates a wide range of local ISS shapes during a cloud's lifetime. Ice crystal PSDs are modified by rapid, local changes in supersaturation. The principal loss path for small ice crystals (radii <10 μm) is sublimation occurring in repeated wave-driven growth-sublimation cycles. Larger crystals are more efficiently removed by sedimentation. According to our simulations, ice crystals in MUT cirrus with radii around 20 μm survive both MTFs and sedimentation removal.

In the presence of GW forcing, a wide range of deposition coefficients describes water vapor uptake on the simulated cirrus ice crystals. Predicting a distribution of deposition coefficients does not appear to strongly influence the simulated supersaturation field. Kinetic growth limitations enhance the frequency of occurrence of supersaturated states in ISSs only slightly relative to the assumption of maximum growth efficiency.

Deposition coefficients are on average larger in TTL than in MUT cirrus. Transition growth produces mostly deposition coefficients >0.01 such that kinetic limitations to growth remain small or moderate. The highest values (>0.1) are found for small ice crystals and high ice supersaturation. Much smaller deposition coefficients are obtained for larger ice crystals close to ice saturation. Therefore, ISSs exhibit weak sensitivity to cloud ice growth from the vapor.

7.2. Remaining Uncertainties and Future Directions

We support the notion that supersaturation- and size-dependent deposition coefficients resolve an apparent contradiction between high versus low values previously inferred from measurements (K. D. Lamb et al., 2022). The fact that overall water vapor uptake is not strongly inhibited suggests that the use of constant, high values (>0.1) for the ice deposition coefficient might be appropriate in cirrus models. We recall that the deposition coefficients used here are particle-averages. Large particle-average values are expected, since, unlike spheres, growth on some of the facets on real ice crystals would be suppressed while others grow rapidly. Thus, these results can be consistent with studies that show inhibited growth of faceted ice. Given experimental uncertainties in measuring s in-situ (at least ± 0.1) and the large variability in local forcing conditions, it may not be possible to evaluate microphysical ice growth models against measured ISSs, strengthening the role of laboratory experiments and physical theory to advance deposition coefficient models for cirrus.

Growth of real ice crystals is more complex than represented by the transition growth model used here, for example, because hollowing and branching can occur, leading to the development of hollow columns and bullet rosettes. Supersaturation and temperature histories also influence the habits of individual ice crystals, which may be parameterized empirically for better estimations of ice crystal fall speeds and optical properties. More work is needed to better characterize deposition coefficients at cirrus temperatures (<233 K). While attachment kinetics may not have a strong, direct influence on the ambient water vapor field according to the current study, variable deposition coefficients likely cause indirect effects that we have not addressed. For instance, a distribution of deposition coefficients means that there could be interesting and important impacts on the size spectrum of ice crystals. Moreover, the habit influence may have some important effects in cloud systems where feedback with habits via ice crystal sedimentation and radiative transfer are allowed. Addressing the importance of these issues calls for future studies.

Our results point to two interrelated key determinants of upper tropospheric ISSs: wave forcing and ice nucleation. Homogeneous freezing of solution droplets appears to be frequently modified by more efficient ice-nucleating particles (Froyd et al., 2022). ISSs are therefore to a large degree determined by local MTFs and competing ice

nucleation (Kärcher, Marcolli, & Mahrt, 2023). However, our GW forcing model does not treat situations nearby deep convection or large topographic barriers. In such cases, updrafts speeds are more transient and may have different spectral characteristics. We expect larger ISS variances and higher mean supersaturation in such situations, with commensurate impacts on cirrus microphysics (Whiteway et al., 2004).

Mesoscale variability in ice supersaturation in cloud-free air is brought about by vertical temperature variability due to GWs (Spichtinger et al., 2005) and by horizontal variability in the moisture field (Fischer et al., 2013). This variability is enhanced within cirrus due to deposition and sublimation processes and remains after cloud dissipation. Systematic statistical analyses of the fine structure of upper tropospheric ice supersaturation outside and within cirrus on $\mathcal{O}$(10 m) spatial and $\mathcal{O}$(1 min) temporal scales are lacking. This poses a challenge for modeling ice supersaturation, for example, in model-based strategies to avoid contrail cirrus formation. Models have not yet been able to demonstrate their ability to predict the small-scale variability in ISSs and the resulting impact on ice cloud microphysics.

The present simulations represent non-uniform growth conditions experienced by size-resolved, settling ice crystal populations as best as possible in an air parcel framework. Although elements of internal cloud dynamics, such as interactive cloud radiation and thermally forced circulations, are missing in this approach, the tools employed here may provide useful stepping stones for future research.

We suggest that future studies employ cirrus models with high spatial and temporal resolution to examine effects of GWs and variable deposition coefficients on cirrus microphysical and optical properties. High resolution global models pinpoint effects on precipitation and cloud radiative effects and life cycles, at the same time revealing how these impact larger-scale processes and circulations. However, such models currently fail to fully capture observed momentum fluxes and associated vertical wind speed variance due to high frequency GWs (Atlas & Bretherton, 2022; Köhler et al., 2023). At scales below the buoyancy length scale (<10–100 m in the upper troposphere), the impact of turbulent motions on ice supersaturation and cirrus formation remains to be investigated.

It is therefore paramount that models properly reproduce the full range of GW forcing, otherwise missing vertical wind speed variability must be parameterized in order to drive ice cloud microphysics. We anticipate that implementing such improvements will also aid efforts directed at mitigating the climate impact of contrail cirrus.

Appendix A: Effect of Sedimentation on Simulated ISSs

Ice crystal settling due to gravity can be treated only approximately in an air parcel framework (Section 3.1). We therefore present results without accounting for size-resolved sedimentation losses. We recall that these losses are, by design, tied to the mean ice crystal radius in each cirrus case such that number concentrations of large ice crystals ($r_j > \bar{r}$) are notably reduced within 5 hr of simulation time, while smaller ice crystals are not as much affected.

Figure A1 shows that including sedimentation leads to an increase in the frequency of occurrence of cirrus states with $s > 0.1$–0.2. This happens because the resulting smaller number concentration of large ice crystals weakens the impact of ice growth relative to simulations without sedimentation in which these crystals leave the parcel.

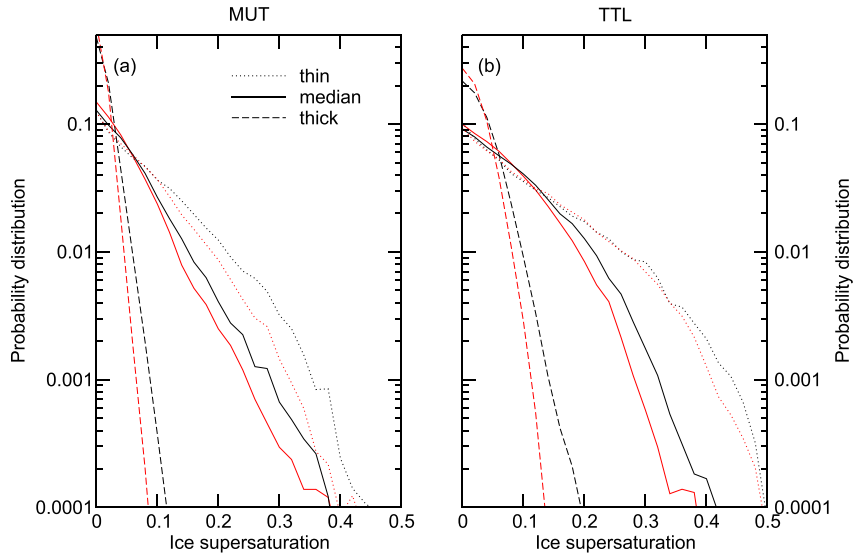

Figure A1. Probability distributions of in-cloud ice supersaturation in the (a) MUT and (b) TTL from numerical simulations based on average forcing ($\sigma_w = 15$ cm s^{-1}) and maximum growth efficiency ($\alpha_j = 1$). Black curves for thin, median, and thick cirrus, respectively, are the ensemble-mean ISSs repeated from Figure 6. The red curves show the corresponding statistics without ice crystal sedimentation.

The effect of sedimentation in our model is generally moderate, because large ice crystals are characterized by small diffusional growth rates. However, as revealed by a comparison to Figure 10, it may compete with or even exceed the effect of ice growth in ensemble-mean ISSs.

Notation

f	Coriolis frequency (s^{-1})
f_K	Kelvin correction
j	index counting the radial size class for ice crystals ($j = 1, \ldots, J$)
ℓ	diffusion length scale (m)
m	parameter specifying the ice crystal growth mechanism
n	(total) ice crystal number concentration (m^{-3})
p	air pressure (Pa)
p_v	water vapor partial pressure
p_{sat}	water vapor pressure at ice saturation
q	cloud ice mass mixing ratio
q_v	water vapor mass mixing ratio
q_{sat}	water vapor mass mixing ratio at ice saturation
r	ice crystal radius (m)
r_c	radius of ice crystal core particle (m)
$\bar{r}$	mean radius of Gamma-distributed ice crystals (m)
s	ambient ice supersaturation
s_{crit}	critical ice supersaturation for ice crystal vapor growth
s_{sfc}	ice supersaturation at the ice crystal surface
t	time (s)
t_a	autocorrelation time for wave-driven vertical wind speeds (s)
t_d	damping time for mesoscale temperature fluctuations (s)
t_q	ice supersaturation quenching time (s)
t_{max}	maximum simulation time (s)
$\bar{v}_v$	mean thermal speed of H_2O molecules in air (m·s^{-1})
w	vertical wind speed (m·s^{-1})
w'	vertical wind speed fluctuation (m·s^{-1})

z	air parcel altitude (m)
D	effective diffusion coefficient ($m^2 \cdot s^{-1}$)
D_v	molecular diffusion coefficient for H_2O in air ($m^2 \cdot s^{-1}$)
F	Gamma (initial ice crystal number-size) distribution
J	maximum number of ice crystal size classes
N	Brunt-Väisälä frequency (s^{-1})
R	random number uniformly distributed over [0,1]
T	air temperature (K)
T'	temperature fluctuation (K)
V	ice crystal terminal fall speed ($m \cdot s^{-1}$)
α	deposition coefficient for uptake of H_2O molecules on ice crystals
δz	sedimentation layer depth (m)
γ	absolute value of the dry adiabatic lapse rate ($K \cdot m^{-1}$)
λ	scale parameter of Gamma distribution (m^{-1})
μ	shape parameter of Gamma distribution
η	ice crystal number mixing ratio (kg^{-1})
ν	cooling/heating rate versus temperature fluctuation amplitude ratio (s^{-1})
ρ	mass density of bulk ice ($kg \cdot m^{-3}$)
ϱ	mass density of air ($kg \cdot m^{-3}$)
σ_w	standard deviation (amplitude) of vertical wind speed fluctuation statistic ($m \cdot s^{-1}$)
Δ	vapor jump distance (m)
Γ	Gamma function
ECMWF	European Centre for Medium-Range Weather Forecasts
GW	gravity wave
ICNC	ice crystal number concentration
ISS	ice supersaturation statistic (probability distribution)
MUT	midlatitude upper troposphere
MTF	mesoscale temperature fluctuation
TTL	tropical tropopause layer
PDF	probability distribution function
PSD	ice crystal number size distribution
RHI	relative humidity over ice

Data Availability Statement

The data records analyzed in this study are available at the NASA Earth Sciences Project Office archive (espoarchive.nasa.gov). Data shown and discussed in this work are available on Zenodo (Kärcher, Jensen, et al., 2023).

Acknowledgments
JYH and GFP were supported by The National Science Foundation under Grant AGS-2128347. JYH was also supported by The U.S. Department of Energy's Atmospheric Science Program Atmospheric Science Research an Office of Science, Office of Biological Environmental Research Program, under Grant DE-SC0021001. Open Access funding enabled and organized by Projekt DEAL.

References

Abramowitz, M., & Stegun, I. A. (1972). *Handbook of mathematical functions*. Dover Publ., Inc.

Alexander, M. J., & Pfister, L. (1995). Gravity wave momentum flux in the lower stratosphere over convection. *Geophysical Research Letters*, *22*(15), 2029–2032. https://doi.org/10.1029/95GL01984

Atlas, R., & Bretherton, C. S. (2022). Aircraft observations of gravity wave activity and turbulence in the tropical tropopause layer: Prevalence, influence on cirrus and comparison with global-storm resolving models. *Atmospheric Chemistry and Physics*, *22*. https://doi.org/10.5194/acp-23-4009-2023

Bacmeister, J. T., Eckerman, S. D., Tsias, A., Carslaw, K. S., & Peter, T. (1999). Mesoscale temperature fluctuations induced by a spectrum of gravity waves: A comparison of parameterizations and their impact on stratospheric microphysics. *Journal of the Atmospheric Sciences*, *56*(12), 1913–1924. https://doi.org/10.1175/1520-0469(1999)056

Burkhardt, U., Kärcher, B., Ponater, M., Gierens, K., & Gettelman, A. (2008). Contrail cirrus supporting areas in model and observations. *Geophysical Research Letters*, *35*(16), L16808. https://doi.org/10.1029/2008GL034056

Corcos, M., Hertzog, A., Plougonven, R., & Podglajen, A. (2021). Observation of gravity waves at the tropical tropopause using superpressure balloons. *Journal of Geophysical Research*, *126*(15), e2021JD035165. https://doi.org/10.1029/2021JD035165

Corcos, M., Hertzog, A., Plougonven, R., & Podglajen, A. (2023). A simple model to assess the impact of gravity waves on ice crystal populations in the Tropical Tropopause Layer. *Atmospheric Chemistry and Physics*, *23*(12), 6923–6939. https://doi.org/10.5194/acp-23-6923-2023

Diao, M., Zondlo, M. A., Heymsfield, A. J., Avallone, L. M., Paige, M. E., Beaton, S. P., et al. (2014). Cloud-scale ice-supersaturated regions spatially correlate with high water vapor heterogeneities. *Atmospheric Chemistry and Physics*, *14*(5), 2639–2656. https://doi.org/10.5194/acp-14-2639-2014

Dzambo, A. M., & Turner, D. D. (2016). Characterizing relative humidity with respect to ice in midlatitude cirrus clouds as a function of atmospheric state. *Journal of Geophysical Research*, *121*(20), 12253–12269. https://doi.org/10.1002/2015JD024643
Feng, Z., Dong, X., Xi, B., McFarlane, S. A., Kennedy, A., Lin, B., & Minnis, P. (2012). Life cycle of midlatitude deep convective systems in a Lagrangian framework. *Journal of Geophysical Research*, *117*(D23), D23201. https://doi.org/10.1029/2012JD018362
Fischer, L., Craig, G. C., & Kiemle, C. (2013). Horizontal structure function and vertical correlation analysis of mesoscale water vapor variability observed by airborne lidar. *Journal of Geophysical Research*, *118*(14), 7579–7590. https://doi.org/10.1002/jgrd.50588
Frank, F. C. (1982). Snow crystals. *Contemporary Physics*, *23*(1), 3–22. https://doi.org/10.1080/00107518208231565
Froyd, K. D., Yu, P., Schill, G. P., Brock, C. A., Kupc, A., Williamson, C. J., et al. (2022). Dominant role of mineral dust in cirrus cloud formation revealed by global-scale measurements. *Nature Geoscience*, *15*(3), 177–183. https://doi.org/10.1038/s41561-022-00901-w
Gierens, K., Matthes, S., & Rohs, S. (2020). How well can persistent contrails be predicted? *Aerospace*, *7*(12), 169. https://doi.org/10.3390/aerospace7120169
Gierens, K., Monier, M., & Gayet, J.-F. (2003). The deposition coefficient and its role for cirrus clouds. *Journal of Geophysical Research*, *108*(D2), 4069. https://doi.org/10.1029/2001JD001558
Gierens, K., Schumann, U., Helten, M., Smit, H., & Marenco, A. (1999). A distribution law for relative humidity in the upper troposphere and lower stratosphere derived from three years of MOZAIC measurements. *Annals of Geophysics*, *17*(9), 1218–1226. https://doi.org/10.1007/s00585-999-1218-7
Gonda, T., & Yamazaki, T. (1978). Initial growth forms of snow crystals growing from frozen cloud droplets. *Journal of the Meteorological Society of Japan*, *62*(1), 190–192. https://doi.org/10.2151/jmsj1965.62.1_190
Haag, W., Kärcher, B., Ström, J., Minikin, A., Lohmann, U., Ovarlez, J., & Stohl, A. (2003). Freezing thresholds and cirrus cloud formation mechanisms inferred from in situ measurements of relative humidity. *Atmospheric Chemistry and Physics*, *3*(5), 1791–1806. https://doi.org/10.5194/acp-3-1791-2003
Hall, W. D., & Pruppacher, H. R. (1976). The survival of ice particles falling from cirrus clouds in subsaturated air. *Journal of the Atmospheric Sciences*, *33*(10), 1995–2006. https://doi.org/10.1175/1520-0469(1976)033%3C1995:TSOIPF%3E2.0.CO;2
Harrington, J. Y., Moyle, A., Hanson, E., & Morrison, H. (2019). On calculating deposition coefficients and aspect ratio evolution in approximate models of ice crystal vapor growth. *Journal of the Atmospheric Sciences*, *76*(6), 1609–1625. https://doi.org/10.1175/JAS-D-18-0319.1
Harrington, J. Y., Sokolowsky, G. A., & Morrison, H. (2021). Semianalytic functions to calculate the deposition coefficients for ice crystal vapor growth in bin and bulk microphysical models. *Journal of the Atmospheric Sciences*, *78*. https://doi.org/10.1175/JAS-D-20-0307.1
Heymsfield, A. J., Miloshevich, L. M., Twohy, C., Sachse, G., & Oltmans, S. (1998). Upper-tropospheric relative humidity observations and implications for cirrus ice nucleation. *Geophysical Research Letters*, *25*(9), 1343–1346. https://doi.org/10.1029/98GL01089
Irvine, E. A., Hoskins, B. J., & Shine, K. P. (2012). The dependence of contrail formation on the weather pattern´and altitude in the North Atlantic. *Geophysical Research Letters*, *39*(12), L12802. https://doi.org/10.1029/2012GL051909
Jackson, R. C., McFarquhar, G. M., Fridlind, A. M., & Atlas, R. (2015). The dependence of cirrus gamma size distributions expressed as volumes in $n_0 - \lambda - \mu$ phase space and bulk cloud properties on environmental conditions: Results from the Small Ice Particles in Cirrus Experiment (SPARTICUS). *Journal of Geophysical Research*, *120*(19), 10351–10377. https://doi.org/10.1002/2015JD023492
Jensen, E. J., Kärcher, B., Ueyama, R., Pfister, L., Bui, T. V., Diskin, G. S., et al. (2018). Heterogeneous ice nucleation in the tropical tropopause layer. *Journal of Geophysical Research*, *123*(21), 12210–12227. https://doi.org/10.1029/2018JD028949
Jensen, E. J., Diskin, G. S., DiGangi, J., Woods, S., Lawson, R. P., & Bui, T. V. (2022). Homogeneous freezing events sampled in the tropical tropopause layer. *Journal of Geophysical Research*, *127*(17), e2022JD036535. https://doi.org/10.1029/2022JD036535
Jensen, E. J., Pfister, L., Bui, T. V., Lawson, P., Baker, B., Mo, Q., et al. (2008). Formation of large ($\simeq$100 μm) ice crystals near the tropical tropopause. *Atmospheric Chemistry and Physics*, *8*(6), 1621–1633. https://doi.org/10.5194/acp-8-1621-2008
Jensen, E. J., Thornberry, T. D., Rollins, A. W., Ueyama, R., Pfister, L., Bui, T. P., et al. (2017). Physical processes controlling the spatial distributions of relative humidity in the tropical tropopause layer over the pacific. *Journal of Geophysical Research*, *122*(11), 6094–6107. https://doi.org/10.1002/2017JD026632
Jensen, E. J., Woods, S., Lawson, R. P., Bui, T. P., Pfister, L., Thornberry, T. D., et al. (2018). Ash particles detected in the tropical lower stratosphere. *Geophysical Research Letters*, *41*(20), 11483–11489. https://doi.org/10.1029/2018GL079605
Kahn, B. H., Gettelman, A., Fetzer, E. J., Eldering, A., & Liang, C. K. (2009). Cloudy and clear-sky relative humidity in the upper troposphere observed by the A-train. *Journal of Geophysical Research*, *114*(D4). https://doi.org/10.1029/2009JD011738
Kärcher, B. (2018). Formation and radiative forcing of contrail cirrus. *Nature Communications*, *9*(1), 1824. https://doi.org/10.1038/s41467-018-04068-0
Kärcher, B., & Burkhardt, U. (2008). A cirrus cloud scheme for general circulation models. *The Quarterly Journal of the Royal Meteorological Society*, *134*(635), 1439–1461. https://doi.org/10.1002/qj.301
Kärcher, B., Dörnbrack, A., & Sölch, I. (2014). Supersaturation variability and cirrus ice crystal size distributions. *Journal of the Atmospheric Sciences*, *71*(8), 2905–2926. https://doi.org/10.1175/JAS-D-13-0404.1
Kärcher, B., & Haag, W. (2004). Factors controlling upper tropospheric relative humidity. *Annals of Geophysics*, *22*(3), 705–715. https://doi.org/10.5194/angeo-22-705-2004
Kärcher, B., Jensen, E., Pokrifka, G., & Harrington, J. (2023). Ice supersaturation statistics in cirrus clouds [Dataset]. Zenodo. https://doi.org/10.5281/zenodo.8210883
Kärcher, B., Marcolli, C., & Mahrt, F. (2023). The role of mineral dust aerosol particles in aviation soot-cirrus interactions. *Journal of Geophysical Research*, *128*(3), D00H02. https://doi.org/10.1029/2022JD037881
Kärcher, B., & Podglajen, A. (2019). A stochastic representation of temperature fluctuations induced by mesoscale gravity waves. *Journal of Geophysical Research*, *124*(21), 11506–11529. https://doi.org/10.1029/2019JD030680
Kärcher, B., Thornberry, T. D., Jensen, E. J., & Krämer, M. (2018). On the statistical distribution of total water in cirrus clouds. *Geophysical Research Letters*, *45*(18), 9963–9971. https://doi.org/10.1029/2018GL079780
Köhler, L., Green, B., & Stephan, C. C. (2023). Comparing Loon superpressure balloon observations of gravity waves in the tropics with global storm-resolving models. *Journal of Geophysical Research*, *128*(15), e2023JD038549. https://doi.org/10.1029/2023JD038549
Korolev, A. V., & Mazin, I. P. (2003). Supersaturation of vater vapor in clouds. *Journal of the Atmospheric Sciences*, *60*(24), 2957–2974. https://doi.org/10.1175/1520-0469(2003)060%3C2957:SOWVIC%3E2.0.CO;2
Krämer, M., Rolf, C., Spelten, N., Afchine, A., Fahey, D., Jensen, E., et al. (2020). A microphysics guide to cirrus – Part 2: Climatologies of clouds and humidity from observations. *Atmospheric Chemistry and Physics*, *20*(21), 12569–12608. https://doi.org/10.5194/acp-20-12569-2020
Krämer, M., Schiller, C., Afchine, A., Bauer, R., Gensch, I., Mangold, A., et al. (2009). Ice supersaturations and cirrus cloud crystal numbers. *Atmospheric Chemistry and Physics*, *9*(11), 3505–3522. https://doi.org/10.5194/acp-9-3505-2009
Lamb, D., & Verlinde, J. (2011). *Physics and chemistry of clouds*. University Press.

Lamb, K. D., Harrington, J. Y., Clouser, B. W., Moyer, E. J., Sarkozy, L., Ebert, V., et al. (2022). Re-evaluating cloud chamber constraints on depositional ice growth in cirrus clouds —- Part 1: Model description and sensitivity tests. *Atmospheric Chemistry and Physics*, *22*. https://doi.org/10.5194/acp-2022-733

Lamquin, N., Stubenrauch, J. C., Gierens, K., Burkhardt, U., & Smit, H. (2012). A global climatology of upper-tropospheric ice supersaturation occurrence inferred from the Atmospheric Infrared Sounder calibrated by MOZAIC. *Atmospheric Chemistry and Physics*, *12*(1), 381–405. https://doi.org/10.5194/acp-12-381-2012

Lee, D. S., Fahey, D. W., Skowron, A., Allen, M. R., Burkhardt, U., Chen, Q., et al. (2021). The contribution of global aviation to anthropogenic climate forcing for 2000 to 2018. *Atmospheric Environment*, *244*, 117834. https://doi.org/10.1016/j.atmosenv.2020.117834

Libbrecht, K. G. (2003). Growth rates of the principal facets of ice between −10°C and −40°C. *Journal of Crystal Growth*, *247*(3–4), 530–540. https://doi.org/10.1016/S0022-0248(02)01996-6

Libbrecht, K. G. (2005). The physics of snow crystals. *Reports on Progress in Physics*, *68*(4), 855–895. https://doi.org/10.1088/0034-4885/68/4/R03

Luo, Z., & Rossow, W. B. (2004). Characterizing tropical cirrus life cycle, evolution, and interaction with upper-tropospheric water vapor using Lagrangian trajectory analysis of satellite observations. *Journal of Climate*, *17*(23), 4541–4563. https://doi.org/10.1175/3222.1

Magee, N., Moyle, A. M., & Lamb, D. (2006). Experimental determination of the deposition coefficient of small cirrus-like ice crystals near −50°C. *Geophysical Research Letters*, *33*(17), L17813. https://doi.org/10.1029/2006GL026665

Magee, N. B., Miller, A., Amaral, M., & Cumiskey, A. (2014). Mesoscopic surface roughness of ice crystals pervasive across a wide range of ice crystal conditions. *Atmospheric Chemistry and Physics*, *14*(22), 12357–12371. https://doi.org/10.5194/acp-14-12357-2014

Mascio, J., McFarquhar, G. M., Hsieh, T.-L., Freer, M., Dooley, A., & Heymsfield, A. J. (2020). The use of gamma distributions to quantify the dependence of cloud particle size distributions in hurricanes on cloud and environmental conditions. *The Quarterly Journal of the Royal Meteorological Society*, *146*(730), 2116–2137. https://doi.org/10.1002/qj.3782

Murphy, D. M., & Koop, T. (2005). Review of the vapour pressures of ice and supercooled water for atmospheric applications. *The Quarterly Journal of the Royal Meteorological Society*, *131*(608), 1539–1565. https://doi.org/10.1256/qj.04.94

Nelson, J., & Baker, M. (1996). New theoretical framework for studies of vapor growth and sublimation of small ice crystals in the atmosphere. *Journal of Geophysical Research*, *101*(D3), 7033–7047. https://doi.org/10.1029/95JD03162

Nelson, J., & Knight, C. (1998). Snow crystal habit changes explained by layer nucleation. *Journal of the Atmospheric Sciences*, *55*(8), 1452–1465. https://doi.org/10.1175/1520-0469(1998)055,1452:SCHCEB.2.0.CO;2

Nelson, J., & Swanson, B. (2019). Lateral facet growth of ice and snow – Part 1: Observations and applications to secondary habits. *Atmospheric Chemistry and Physics*, *19*(24), 15285–15320. https://doi.org/10.5194/acp-19-15285-2019

O'Shea, S. J., Choularton, T. W., Lloyd, G., Crosier, J., Bower, K. N., Gallagher, M., et al. (2016). Airborne observations of the microphysical structure of two contrasting cirrus clouds. *Journal of Geophysical Research*, *121*(22), 13510–13536. https://doi.org/10.1002/2016JD025278

Petzold, A., Neis, P., Rütimann, M., Rohs, S., Berkes, F., Smit, H. G. J., et al. (2020). Ice-supersaturated air masses in the northern mid-latitudes from regular in situ observations by passenger aircraft: Vertical distribution, seasonality and tropospheric fingerprint. *Atmospheric Chemistry and Physics*, *20*(13), 8157–8179. https://doi.org/10.5194/acp-20-8157-2020

Podglajen, A., Hertzog, A., Plougonven, R., & Legras, B. (2016). Lagrangian temperature and vertical velocity fluctuations due to gravity waves in the lower stratosphere. *Geophysical Research Letters*, *43*(7), 3543–3553. https://doi.org/10.1002/2016GL068148

Podglajen, A., Hertzog, A., Plougonven, R., & Legras, B. (2020). Lagrangian gravity wave spectra in the lower stratosphere of current (re)analyses. *Atmospheric Chemistry and Physics*, *20*(15), 9331–9350. https://doi.org/10.5194/acp-20-9331-2020

Pokrifka, G. F., Moyle, A. M., Hanson, L. E., & Harrington, J. Y. (2020). Estimating surface attachment kinetic and growth transition influences on vapor-grown ice crystals. *Journal of the Atmospheric Sciences*, *70*(7), 2393–2410. https://doi.org/10.1175/JAS-D-19-0303.1

Pokrifka, G. F., Moyle, A. M., & Harrington, J. Y. (2023). Effective density derived from laboratory measurements of the vapor growth rates of small ice crystals at −65 to −40°C. *Journal of the Atmospheric Sciences*, *80*(2), 501–517. https://doi.org/10.1175/JAS-D-22-0077.1

Reutter, P., Neis, P., Rohs, S., & Sauvage, B. (2020). Ice supersaturated regions: Properties and validation of ERA-interim reanalysis with IAGOS in situ water vapour measurements. *Atmospheric Chemistry and Physics*, *20*(2), 787–804. https://doi.org/10.5194/acp-20-787-2020

Rollins, A. W., Thornberry, T. D., Gao, R. S., Woods, S., Lawson, R. P., Bui, T. P., et al. (2016). Observational constraints on the efficiency of dehydration mechanisms in the tropical tropopause layer. *Geophysical Research Letters*, *43*(6), 2912–2918. https://doi.org/10.1002/2016GL067972

Satoh, M., Stevens, B., Judt, F., Khairoutdinov, M., Lin, S.-J., Putman, W. M., & Düben, P. (2019). Global cloud-resolving models. *Current Climate Change Reports*, *5*(3), 172–184. https://doi.org/10.1007/s40641-019-00131-0

Spichtinger, P., Gierens, K., & Dörnbrack, A. (2005). Formation of ice supersaturation by mesoscale gravity waves. *Atmospheric Chemistry and Physics*, *5*, 1243–1255. https://doi.org/10.5194/acp-5-1243-2005

Spichtinger, P., Gierens, K., Smit, H. G. J., Ovarlez, J., & Gayet, J.-F. (2004). On the distribution of relative humidity in cirrus clouds. *Atmospheric Chemistry and Physics*, *4*(3), 639–647. https://doi.org/10.5194/acp-4-639-2004

Ström, J., Seifert, M., Kärcher, B., Ovarlez, J., Minikin, A., Gayet, J.-F., et al. (2003). Cirrus cloud occurrence as function of ambient relative humidity: A comparison of observations obtained during the INCA experiment. *Atmospheric Chemistry and Physics*, *3*(5), 1807–1816. https://doi.org/10.5194/acp-3-1807-2003

Thornberry, T. D., Rollins, A. W., Avery, M. A., Woods, S., Lawson, R. P., Bui, T. V., & Ga, R.-S. (2017). Ice water content-extinction relationships and effective diameter for TTL cirrus derived from in situ measurements during ATTREX 2014. *Journal of Geophysical Research*, *122*(8), 4494–4507. https://doi.org/10.1002/2016JD025948

Whiteway, J., Cook, C., Gallagher, M., Choularton, T., Harries, J., Connolly, P., et al. (2004). Anatomy of cirrus clouds: Results from the Emerald airborne campaigns. *Geophysical Research Letters*, *31*(24), L24102. https://doi.org/10.1029/2004GL021201

Wood, S. E., Baker, M. B., & Calhoun, D. (2001). New model for the vapor growth of hexagonal ice crystals in the atmosphere. *Journal of Geophysical Research*, *106*(D5), 4845–4870. https://doi.org/10.1029/2000JD900338

Zhang, C., & Harrington, J. Y. (2014). Including surface kinetic effects in simple models of ice vapor diffusion. *Journal of the Atmospheric Sciences*, *71*(1), 372–390. https://doi.org/10.1175/JAS-D-13-0103.1

Zhao, M., & Shi, X. (2023). A study on the wide range of relative humidity in cirrus clouds using large-ensemble parcel model simulations. *Atmosphere*, *14*(3), 583. https://doi.org/10.3390/atmos14030583